European Journal of Chemistry

View Journal Online
View Article Online

Cytotoxicity evaluation and DNA binding studies of 1,3-dihydroxy-2-(4-methoxyphenyl)-4,5-dimethyl-1*H*-imidazol-3-ium chloride beyond its structural and Hirshfeld surface analysis, spectroscopic investigations, vibrational assignments and theoretical characterizations

Munna Mukhia [1], Sumiran Tamang [1], Koushik Chakraborty [1], Imran Habib [2], Koustav Singha [2], Sangita Dey [3], Anoop Kumar [3], Dhiraj Brahman [4], Mossaraf Hossain [2,*], and Kiran Pradhan [1,*]

[1] *Department of Chemistry, University of North Bengal, Raja Rammohunpur, District-Darjeeling, 734013, India*
[2] *Synthetic Organic Research Laboratory, University Grants Commission-Human Resource Development Centre (Chemistry), University of North Bengal, District-Darjeeling, 734013, India*
[3] *Department of Biotechnology, University of North Bengal, Raja Rammohunpur, District- Darjeeling, 734013, India*
[4] *Department of Chemistry, St. Joseph's College, Post Office-North Point, District-Darjeeling, 734104, India*

* *Corresponding author at: K.P.: Department of Chemistry, University of North Bengal, Raja Rammohunpur, District-Darjeeling, 734013, India; M.H.: Synthetic Organic Research Laboratory, University Grants Commission-Human Resource Development Centre (Chemistry), University of North Bengal, District-Darjeeling, 734013, India.*
e-mail: kpradhan@nbu.ac.in (K. Pradhan), mossarafchem@nbu.ac.in (M. Hossain).

RESEARCH ARTICLE

doi 10.5155/eurjchem.17.1.40-61.2726

Received: 22 November 2025
Received in revised form: 23 January 2026
Accepted: 25 January 2026
Published online: 31 March 2026
Printed: 31 March 2026

KEYWORDS

DFT
Cytotoxicity
DNA binding
Crystal structure
Hirshfeld surface analysis
1,3-Dihydroxy imidazolium chloride

ABSTRACT

1,3-Dihydroxy-2-(4-methoxyphenyl)-4,5-dimethyl-1*H*-imidazol-3-ium chloride (DMPDI) was synthesized via a solvent-free protocol and characterized. Crystallographic analyzes reveal that the crystal cation, as a result of steric hindrance, is not planar; the imidazole ring system has a dihedral angle of 44.62° with the plane of the anisole group. The molecule was also optimized using the density functional theory formalism, with the B3LYP functional and 6-31G+(d,2p) basis set. The computationally simulated IR, Raman, and NMR spectra were compared with the corresponding experimental data and detailed frequency assignments were performed. Additionally, frontier molecular orbitals (FMO), molecular electrostatic potential (MEP), and nonlinear optical (NLO) properties were calculated using density functional theory (DFT) methods. Evaluation of the antiproliferative activity of the compound revealed potent anticancer activity with IC_{50} values of 458.6 µM (124.18 µg/mL) and 645.7 µM (174.78 µg/mL) performed *in vitro* with A-549 lung cancer and SKOV-3 ovarian cancer cell lines, respectively. The compound was found to be less toxic to the normal hepatic cell line (WRL-68). The selectivity index (SI) of the compound was calculated and found to be 2.5 and 1.8 for A-549 and SKOV3, respectively. Molecular docking studies with human Topoisomerase I (PDB ID: 1RRJ) were carried out to assess binding affinity and investigate the possible mechanism behind the observed anticancer effect. Preliminary binding studies with calf thymus DNA (CT-DNA) by absorption titration and displacement studies with ethidium bromide revealed that DMPDI effectively binds via groove binding. For the theoretical investigation of DNA binding interactions, docking studies of DMPDI with B-DNA dodecamer (PDB ID: 1BNA) were carried out to validate the experimental results.

Cite this: *Eur. J. Chem.* **2026**, *17(1)*, 40-61 **Journal website**: www.eurjchem.com

1. Introduction

Imidazole is considered one of the most privileged scaffolds among heterocycles due to its broad spectrum of biological activities [1-3]. In addition to being present in nature in the form of a structural component of histidine, vitamin B12, purines and alkaloids, the imidazole scaffold is also present in the structure of many synthetic drug molecules, for example dacarbazine [4], ketoconazole [5], losartan [6], cimetidine [7], azomycin [8], among many others. Furthermore, its N-oxide and N-hydroxy derivatives [9,10] have also been found to have a multitude of applications. *N*-oxides and *N*-hydroxysubstituted imidazoles and benzimidazoles are valuable synthons in the design and synthesis of molecular structures with the imidazole scaffold [11,12]. Of late, they have steadily gained interest as potential biologically active compounds. Studies have found that 1-hydroxyimidazole derivatives have the potential to act as herbicides, nematocides, insecticides, fungicides, antiparasitary agents, and can also exhibit bacteriostatic properties [13-16]. Furthermore, they have also been found to exhibit anti-protozoal [17], antitumor [18,19], and antiviral [20] activity. Studies have also revealed these molecules as potential selective inhibitors of various kinases [21], as well as potential hypotensive drugs [22].

https://dx.doi.org/10.5155/eurjchem.17.1.40-61.2726

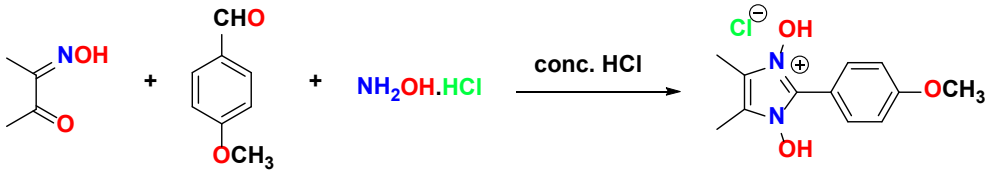

Scheme 1. Synthesis of 1,3-dihydroxy-2-(4-methoxyphenyl)-4,5-dimethyl-1*H*-imidazol-3-ium chloride (DMPDI).

In view of the growing interest in the field of medicinal chemistry, the chemistry of 1-hydroxy imidazole-3-oxide has also become very significant. Much of our previous studies were restricted to the synthesis, characterization, and theoretical studies of the above compounds. During our work with these essential scaffolds, it was found that a slight change in the reagent and preparation conditions led to the formation of 1,3-dihydroxy imidazolium salts instead of the 1-hydroxy imidazole-3-oxides. Although there is the presence of only a hydrogen and a chlorine atom in excess in the former salts, we envisaged that this would bring about a change in the molecular structure as a well as significant change in the properties of the scaffold. Thus, in the present study, the crystal structure of 1,3-dihydroxy-2-(4-methoxyphenyl)-4,5-dimethyl-1*H*-imidazol-3-ium chloride (DMPDI) is reported along with its Hirshfeld surface analysis. DFT calculations were further performed to compare the geometry of the title compound with its crystal data. Moreover, the *N*-hydroxyimidazolium compound is studied in detail for its structure and other physicochemical properties. Experimental IR and Raman spectra are compared with the computationally simulated scaled spectra, followed by detailed frequency assignments. ^{1}H NMR studies and the first and second hyperpolarizabilities are also reported. The highest occupied molecular orbital (HOMO) and lowest unoccupied molecular orbital (LUMO) energy values were calculated, and other reactivity descriptors were studied. The molecular electrostatic potential (MEP) is computed to confirm the interactive forces that bind with the target compound.

More importantly, the anticancer properties of DMPDI were evaluated with the help of in vitro experiments against a few cell lines, *viz*. human lung cancer (A-549) and human ovarian cancer (SKOV-3) cell lines. Furthermore, to evaluate its selectivity, its toxicity against the normal hepatic cell line (WRL-68) was also determined. Furthermore, DNA binding studies were also carried out to substantiate our findings from the cytotoxicity studies, employing UV-vis absorption titration, ethidium bromide displacement assay, and molecular docking analysis. We investigated the activity of the compound DMPDI to inhibit Topoisomerase 1 by molecular docking. Topoisomerases play an important role in DNA replication, transcription, mitotic chromosome formation, DNA recombination, and pre-mRNA splicing [23,24]. Topo 1 has been found to be elevated in malignant tumors, including carcinomas of the lung [25]. Thus, this study also describes a molecular docking analysis to show the potential of the title compound against human topoisomerase I receptor protein (1RRJ), a well-known target for anticancer agents.

In summary, this manuscript presents the preparation, crystal structure, detailed spectral analysis, quantum mechanical properties, various physicochemical applications, and biological utility of 1,3-dihydroxy-2-(4-methoxyphenyl)-4,5-dimethyl-1*H*-imidazol-3-ium chloride. To the best of our knowledge, the crystal structure of the title compound, its antiproliferative activity, and DNA binding studies are reported for the first time in this paper.

2. Experimental

2.1. Materials

All reagents were obtained from Aldrich Chemicals, TCI, and Thomas Baker and were used without further purification. Solvents were purchased from commercial sources and used after standard distillation. Thin layer chromatography (TLC) was performed on Merck silica gel 60F_{254} plates.

2.2. Instrumentation

^{1}H (500 MHz) and ^{13}C (126 MHz) NMR data were recorded in DMSO-d_6 using tetramethyl silane (TMS), an internal standard on a Bruker Avance 500 spectrometer. The chemical shift values (δ) are expressed in parts per million (ppm), while the coupling constant (J) is expressed in Hz. The FT-IR spectrum was recorded using KBr pellets on a Bruker Alpha II spectrometer (Ettlingen, Germany) in the 4000-400 cm^{-1} region. Raman measurements were conducted using EnSpectr R532 Raman microscope equipment. The excitation source was the Olympus CX41 microscope, which has a wavelength of 532 nm and a maximum laser power of 50 mW. The Levenhuk C310 NG was used for viewing, and a 20× objective lens was installed on the microscope for sample focusing. The electrospray mass spectrum was recorded on a MICROMASS QUATTRO II triple quadruple mass spectrometer. The ESI capillary was set at 3.5 kV and the cone voltage was 40 V. UV-visible absorption spectra were recorded using a UV-VIS spectrophotometer (UV-1900 Series, Shimadzu, Model UV1900I, Serial No. A12536285177), operated with LabSolutions UV-Vis software. Measurements were carried out using quartz cuvettes with a 10-mm path length over the wavelength range of 200-800 nm at room temperature. Fluorescence emission spectra were recorded using a Photon Technology International (PTI) spectrofluorometer (Serial No. 3040) at room temperature using quartz cuvettes with a 10-mm path length and a slit width of 2 mm for both excitation and emission.

2.3. Synthesis of 1,3-dihydroxy-2-(4-methoxyphenyl)-4,5-dimethyl-1H-imidazol-3-ium chloride (DMPDI)

The synthetic route to the title compound, DMPDI is illustrated in Scheme 1. It was synthesized by a slight modification of our previously reported [26] solvent-free procedure. 2 mmol (0.202 g) of diacetyl monoxime was thoroughly ground with 2 mmol (0.272 g) of 4-methoxybenzaldehyde and 10 mmol (0.695 g) of hydroxylamine hydrochloride in an agate mortar and pestle for 3 minutes. The mixture was then transferred to a 25 mL round bottom flask and 2 mmol of conc. HCl was added. It was heated in an oil bath maintained at 110-120 °C with constant stirring for another 7 min. The formation of the product was confirmed by thin layer chromatography (TLC) using 0.25 mm Merck Aluminum silica gel 60F_{254} pre-coated plates. The reaction mixture was cooled to room temperature and 5 mL of diethyl ether was added. A white-colored precipitate was obtained. The product was then washed with ethyl acetate to obtain the pure product (ESI, Figure S1-S3).

1, 3-Dihydroxy-2-(4-methoxyphenyl)-4, 5-dimethyl-1H-imidazol-3-ium chloride (DMPDI): M.p.: 165-168 °C (uncorrected). ^{1}H NMR (500 MHz, DMSO-d_6, δ, ppm): 13.51 (s, 2H, broad, N-OH), 7.93 (d, J = 8.4 Hz, 2H, ArH), 7.19 (d, J = 8.5 Hz, 2H, ArH), 3.86 (s, 3H, OCH_3), 2.26 (s, 6H, CH_3). ^{13}C NMR (126 MHz, DMSO-d_6, δ, ppm): 160.93, 133.64, 130.69, 121.21, 113.78, 111.45, 54.95, 6.50. LC-MS (m/z): $[M]^+$ calcd. for $C_{12}H_{15}N_2O_3^+$ 235.108; found, 235.238.

2.4. Crystallographic study

A suitable single crystal of 1,3-dihydroxy-2-(4-methoxy phenyl)-4,5-dimethyl-1*H*-imidazol-3-ium chloride (DMPDI) for X-ray diffraction was mounted on a Bruker SMART-APEX CCD diffractometer and the diffraction data were collected using monochromatic Mo Kα radiation (λ = 0.71073 Å) with the ω and φ scan technique. The unit cell was determined using Bruker SMART, the diffraction data were integrated with the Bruker SAINT system, and the data were corrected for absorption using SADABS [27]. The structure was solved by the direct method and was refined by full matrix least squares based on F^2 using SHELXL 97 [28]. All H atoms were localized from the difference electron density map and refined isotropically. The ORTEP plot and the packing diagram were generated with ORTEP-3 for Windows [29] and PLATON [30]. WinGX [31] was used to prepare the material for publication. A CIF file containing complete information of the studied structure was deposited with CCDC, deposition number 2183509, and is freely available upon request from the Director, CCDC, 12 Union Road, Cambridge CB2 1EZ, UK (Fax:+44-1223-336033; e-mail: deposit@ccdc.cam.ac.uk).

2.5. Hirshfeld surface analysis

Hirshfeld surfaces and 2D fingerprint plots were generated using Crystal Explorer 21.5. The X-ray single-crystal crystallographic information file of DMPDI was used as the input file.

2.6. Computational methods

The molecular geometry, frontier molecular orbitals (HOMO and LUMO), nonlinear optical properties (NLO), NMR parameters and vibrational frequencies of the compound were optimized using Density Functional Theory (DFT) at the B3LYP/6-31G+(d,2p) level, employing Becke's three-parameter hybrid method (B3) with the Lee-Yang-Parr (LYP) correlation functional [32,33]. All calculations were carried out with the Gaussian 16, Revision A.03 software package, and the results were visualized using GaussView 6.0 [34] on an HP Z640 desktop equipped with an Intel Xeon E5-2630 V4 processor (2.2 GHz).

2.7. Antiproliferative activity studies

Antiproliferative activity studies of the target molecule DMPDI were performed according to the procedure described in the literature [35]. The lung cancer cell lines (A549), human ovarian carcinoma (SKOV3), and human normal liver (WRL-68) cell lines were purchased from the National Centre for Cell Science (NCCS), Pune, India (NCCS, India). Sodium bicarbonate, MEM (Minimum Essential Medium Eagle) media, Cell culture tested 10×PBS, 10×Trypsin EDTA solution, isopropanol, Petri dishes, and 96 well plates were purchased from HiMedia, India Merck, India, and Tarsons, India. MTT [3-(4,5-dimethylthiazol-2-yl)-2,5 diphenyltetrazolium bromide] dye was purchased from Bio Basic Canada Inc., Canada.

2.7.1. Cell culture

Lung cancer cell lines (A549) were cultured in Dulbecco's modified Eagle's Medium-high-glucose (DMEM) supplemented with 10% fetal bovine serum (FBS) and 1% glutamax. Human ovarian carcinoma (SKOV3) and human normal liver (WRL-68) cell lines were cultured separately in MEM media, which was supplemented with 10% FBS, 100 units/mL of penicillin, 100 µg/mL of streptomycin and 2.2 g/L of sodium bicarbonate in 100 mm Petri dishes in a humified incubator containing 5% CO_2 at 37 °C. 80-90% confluent plates were passaged twice a week.

2.7.2. Cell viability assay (MTT assay)

In a 96-well microtiter plate, approximately 100 µL of media containing cells were seeded at a density of 5×10^3 cells per well and incubated overnight at 37 ° C in a humidified incubator containing 5% CO_2. Following attachment, the sample DMPDI (dissolved in DMSO) was added at concentrations of 50, 100, 150, 200, and 250 µg/mL in triplicate manner and placed under the same conditions for 24 hours. The day after incubation, the media was discarded, and 10 µL of freshly prepared MTT dye solution (Stock solution 5 mg/mL, dissolved in 1× PBS) was added to each well and incubated for another 3 hours under the same conditions. After 3 hours, 50 µL of isopropanol was added to each well to solubilize the purple formazan crystal, and it was gently agitated for a few minutes. The absorbance was measured at 620 nm by a Spectro Star Nano Spectrophotometer. The percentage of cytotoxicity was calculated as,

$$\text{Percentage of cytotoxicity (\%)} = \frac{(Y-X)}{Y} \times 100 \quad (1)$$

where X is the mean OD of cells treated with different concentrations of samples and Y is the mean OD of cells treated with DMSO, since the samples were dissolved in DMSO. IC_{50} values were calculated using GraphPad Prism Software 5 and are expressed as mean ± Standard deviation.

2.8. Molecular docking study

Auto Dock Vina 1.2.7 [36,37] was used to perform molecular docking studies to evaluate the binding affinity of DMPDI with human topoisomerase I. The crystal structure of human topoisomerase I (PDB ID: 1RRJ), refined at 2.30 Å, was downloaded from the RCSB Protein Data Bank (https://www.rcsb.org/structure/1RRJ). The dock prep module of UCSF Chimera 1.19 [38] was used to prepare the protein by removing water molecules, converting selenomethionine to methionine, adding hydrogens, and repairing incomplete side chains. The Kollman method was used to calculate and add the partial charges using Auto Dock Tools (ADT) 1.5.7 [39] and convert it to an Autodock compatible file. The UCSF Chimera was used to determine the geometric center of the cocrystallized ligand in the protein structure, obtaining the coordinates of the center of the grid (x = 4.590, y = -4.900, and z = 9.550). A grid size of 40×40×40 Å was used for the docking study. The optimized structure of the title molecule at the B3LYP/6-31G+(d,2p) level of basis set was used as the ligand, which was further prepared by adding Gasteiger charges and merging nonpolar hydrogens using ADT. The best-scoring pose of the ligand, as suggested by Vina, was selected and the interaction site was visually examined. The docking protocol was validated by redocking the co-crystallized ligand in the active site, producing an RMSD value within acceptable limits (< 2.0 Å). The same protocol was followed for docking of DMPDI with the B-DNA dodecamer (PDB ID: 1BNA), with the grid center coordinates as x = 14.778, y = 20.974, and z = 8.806 and the grid size 40×40×40 Å.

Table 1. Crystal data collection and structure refinement for DMPDI.

Crystal data	Value
CCDC reference number	2183509
Empirical formula	$C_{12}H_{15}N_2O_3Cl$
Moiety formula	$C_{12}H_{15}N_2O_3$, Cl
Formula weight	270.71
Crystal system	Monoclinic
Space group	$P2_1/n$
Colour, habit	Off-white, rod
Size, mm	0.28 × 0.26 × 0.25
Unit cell dimensions	
a = 8.5143(4)Å	α = 90°
b = 7.6289(4)Å	β = 94.228(4)°
c = 20.1962(9)Å	γ = 90°
Volume Å^3	1308.27(11)
Z	4
Density (calculated), Mg/m^3	1.374
Absorption coefficient, mm^{-1}	0.294
F(000)	568
Data collection	
Temperature, K	293(2)
Theta range for data collection	3.35° to 25.00°
Index ranges	$-10 \le h \le 9$
	$-7 \le k \le 9$
	$-24 \le l \le 23$
Reflections collected	5168
Unique reflections	2299
Observed reflections (>2$\sigma(I)$)	1890
R_{int}	0.0169
Completeness to θ, %	25.00°, 99.8
Absorption correction	Multi-scan (SADABS; Bruker, 2000)
	T_{min} = 0.922, T_{max} = 0.923
Refinement	
Refinement method	Full-matrix least-squares on F^2
Data / restraints / parameters	2299 / 0 / 223
Calculated weights, w	$1/[\sigma^2(F_o^2) + (0.0378P)^2 + 0.3138P]$ where $P = (F_o^2 + 2F_c^2)/3$
Goodness-of-fit on F^2	1.051
Final R indices [I > 2σ(I)]	R_1 = 0.0356, wR_2 = 0.0843
R indices (all data)	R_1 = 0.0456, wR_2 = 0.0909
Largest diff. peak and hole	0.169 and -0.199 e.Å^{-3}

The 2D and 3D interaction diagrams were captured using BIOVIA Discovery Studio Visualizer v24.1.0.23298 [40].

2.9. DNA interaction studies

2.9.1. UV-vis absorption titration

For the absorption study, DMPDI and ct-DNA were used following the reported methodology [41]. A 50 mM CT-DNA solution was prepared in tris-HCl buffer (pH = 7.2), and a 1×10^{-4} M DMPDI solution in DMSO. The absorption titration was performed by aliquot addition of ct-DNA solution to the DMPDI solution, while keeping its concentration fixed, and absorption spectra were recorded for each addition. The spectra obtained were used to analyze the interaction of DMPDI with CT-DNA using the Wolfe-Shimmer equation (Equation 2):

$$[DNA]/(\varepsilon_a - \varepsilon_f) = [DNA]/(\varepsilon_b - \varepsilon_f) + 1/K_b(\varepsilon_b - \varepsilon_f) \quad (2)$$

where [DNA] denote the concentration of DNA, ε_f and ε_b represent the extinction coefficient for free and bound DNA, respectively, while ε_a is the extinction coefficient of the compound at a given concentration of DNA. The ratio of the slope to the intercept in the $[DNA]/(\varepsilon_a - \varepsilon_f)$ against [DNA] graph was used to calculate the intrinsic binding constant (K_b) [42].

2.9.2. Ethidium bromide (EB) displacement assay

To a 3 mL solution of CT-DNA (2 μM) prepared in tris-HCl buffer (pH = 7.2), 1×10^{-5} mL of ethidium bromide (EB) was added. The fluorescence spectrum of the EB-DNA complex was recorded (λ_{ex} = 440 nm, λ_{em} = 450-800 nm) at first, followed by incremental addition (10-200 μM) of 1×10^{-4} M solution of DMPDI, with the spectra recorded for each addition. The Stern-Volmer equation was used to quantitatively evaluate the resultant fluorescence spectrum [43], represented by Equation 3,

$$I_0/I = K_{sv}[Q] + 1 \quad (3)$$

where I_0 and I denote the emission intensities in the absence and presence of the quencher, K_{sv} is the quenching constant, and [Q] represents the concentration of DMPDI.

3. Results and discussion

3.1. Molecular and crystal structure

The molecular and crystal structure of DMPDI was investigated to elucidate its geometrical features, bonding interactions, and packing arrangement in the solid state. The compound 1,3-dihydroxy-2-(4-methoxyphenyl)-4,5-dimethyl-1*H*-imidazol-3-ium chloride (DMPDI) crystallizes in the monoclinic $P2_1/n$ space group. Detailed crystallographic data and experimental parameters for DMPDI are presented in Table 1. The selected bond lengths and torsion angles are presented in Table 2. The asymmetric unit, consisting of a 1,3-dihydroxy-2-(4-methoxyphenyl)-4,5-dimethyl-1*H*-imidazol-3-ium cation and a chloride anion, is shown in Figure 1. The molecule is not a planar molecule, as is evident from the torsion angles around the C1–C8 bond. There is puckering in the C1–C8 bond. The puckering is envisioned by the dihedral angle between the planes containing the phenyl and imidazole moiety, which is *ca.* 44.62°. Anisotropic displacement parameters (ADPs) for all nonhydrogen atoms are provided in the Supplementary Information (CIF file) (ESI, Table S3). The ADP values suggest a well-ordered crystal structure with moderate atomic thermal motion.

Table 2. Comparison of the optimised geometrical parameters (BLYP/631G+(d,2p)) of 1,3-dihydroxy-2-(4-methoxyphenyl)-4,5-dimethyl-1*H*-imidazol-3-ium chloride, with X-ray single crystal data, atom labelling according to Figure 1.

Bond lengths (Å)	Theoretical	Experimental	Bond angles (°)	Theoretical	Experimental
O3-C7	1.432	1.429(3)	C4-O3-C7	119.60232	118.54(17)
C4-O3	1.341	1.361(2)	O3-C4-C5	115.67548	115.83(17)
C4-C5	1.41	1.387(3)	O3-C4-C3	124.84447	124.36(18)
C5-C6	1.38	1.381(3)	C4-C3-C2	119.76686	119.48(19)
C6-C1	1.416	1.394(2)	C4-C5-C6	120.56427	120.64(18)
C1-C2	1.408	1.383(3)	C3-C4-C5	119.48005	119.80(18)
C2-C3	1.387	1.389(3)	C5-C6-C1	120.44532	119.99(19)
C3-C4	1.407	1.380(3)	C2-C1-C6	118.58668	118.92(17)
C1-C8	1.448	1.459(2)	C1-C2-C3	121.15539	121.17(18)
C8-N1	1.357	1.341(2)	C6-C1-C8	120.53189	121.55(17)
N1-C9	1.394	1.383(2)	C2-C1-C8	120.87871	119.53(16)
C9-C10	1.368	1.357(2)	C1-C8-N2	128.92262	127.44(16)
C10-N2	1.396	1.378(2)	C1-C8-N1	128.3487	129.17(15)
N2-C8	1.358	1.340(2)	N1-C8-N2	102.72846	103.37(14)
N1-O1	1.372	1.380(18)	O2-N2-C8	122.80625	123.35(14)
N2-O2	1.375	1.371(18)	N1-C9-C10	105.55759	105.69(15)
C10-C12	1.489	1.487(3)	O1-N1-C9	122.4579	124.14(14)
			C9-C10-N2	105.74316	105.69(15)
			C10-N2-C8	112.79524	112.77(14)
			C9-N1-C8	112.79524	112.49(14)
			C10-N2-O2	122.64276	123.46(14)
			N1-C9-C11	121.88888	122.86(17)
			C10-C9-C11	132.55353	131.37(18)
			N2-C10-C12	121.7433	122.27(17)
			C9-C10-C12	132.51309	132.00(18)
Torsion angles (°)	**Theoretical**	**Experimental**	**Torsion angles (°)**	**Theoretical**	**Experimental**
C7-O3-C4-C5	179.4082	176.32(2)	C2-C1-C8-N1	-148.888	-135.06(19)
C7-O3-C4-C3	-0.60201	-2.26(3)	C2-C1-C8-N2	31.3094	42.88(3)
O3-C4-C5-C6	-179.8907	-178.24(19)	C1-C8-N2-C10	176.685	177.89(16)
O3-C4-C3-C2	179.7771	177.74(19)	C1-C8-N2-O2	11.438	8.97(3)
C4-C3-C2-C1	0.43392	0.51(3)	C1-C8-N1-C9	-177.283	-178.28(17)
C4-C5-C6-C1	0.23517	0.26(3)	C1-C8-N1-O1	-1.6195	-0.26(3)
C5-C6-C1-C8	179.36473	178.28(18)	C8-N1-C9-C11	178.9312	178.20(18)
C3-C2-C1-C8	-179.6999	-178.69(18)	C8-N1-C9-C10	1.0664	0.29(2)
C6-C1-C8-N1	31.7203	46.12(3)	C8-N2-C10-C12	-177.1466	-176.32(17)
C6-C1-C8-N2	-148.088	-135.93(2)	C8-N2-C10-C9	2.63788	0.62(2)

Table 3. Hydrogen-bonded geometries in DMPDI *.

Bond	D – H (Å)	H···A (Å)	D···A (Å)	D - H···A (°)
O1–H1···Cl1 [i]	0.88(3)	2.10(3)	2.9732(16)	172(2)
O2–H2A···Cl1 [ii]	1.00(3)	1.95(3)	2.9393(14)	170(2)

* Symmetry codes: (i) -1+*x*, *y*, *z*; (iii) 3/2-*x*, 1/2+*y*, 1/2-*z*.

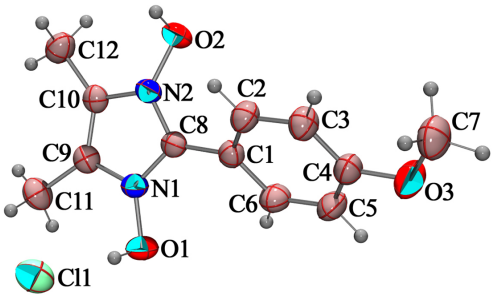

Figure 1. Asymmetric unit of DMPDI with displacement ellipsoids drawn at 50% probability level.

Atoms O3 and C7 show slightly higher displacement parameters, suggesting increased vibrational flexibility in these regions, which is consistent with the ORTEP diagram drawn at the 50% probability level (Figure 1). Overall, these observations support the quality and reliability of the refined crystal structure.

3.2. Supramolecular features

The three-dimensional packing arrangement of DMPDI is presented in Figure 2. In the crystal, there are two intermolecular O–H···Cl interactions (Table 3, Figure 3). Each cation is found with form two hydrogen bonds to chloride anions, which stabilizes the crystal packing. The crystal is further stabilized by an intermolecular C–H···*Cg* interaction (Table 4, Figure 4) between C12–H12B and *Cg*2 (centroid of the C1 – C6 ring).

3.3. Hirshfeld surface analysis

Hirshfeld Surface Analysis is one of the most powerful tools for the visualization and evaluation of the effect of close-range interactions. The quantitative ratios of atom-to-atom short contacts with the potential to form weak hydrogen-bond intermolecular interactions, as well as the locations of these interactions, are significantly revealed by Hirshfeld surface analysis [44]. Red spots on the Hirshfeld surface indicate short contacts. Figure 5 represents the surface that has been mapped over the d_{norm} for the complex DMPDI. Dark red regions represent strong molecular interactions, and light red spots show weak intermolecular interactions.

Table 4. X–H···*Cg* interactions in DMPDI *.

X–H···*Cg*	H···*Cg* (Å)	H_{perp} (Å)	γ (°)	X–H···*Cg* (°)	X···*Cg* (Å)
C12–H12B···*Cg*2 iii	2.93(2)	2.92	4.19	133.2(18)	3.669(2)

* Symmetry codes: (iii) 1/2-*x*, -1/2+*y*, 1/2-*z*; *Cg*2 is the centroid of the C1–C6 ring.

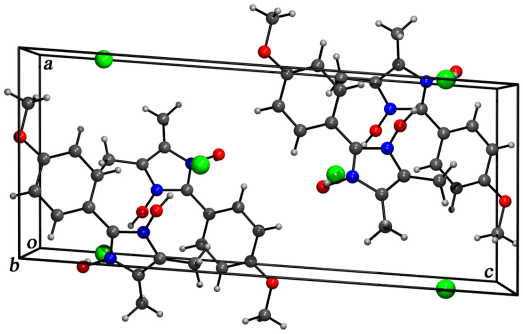

Figure 2. Molecular arrangement of DMPDI in the *ac* plane.

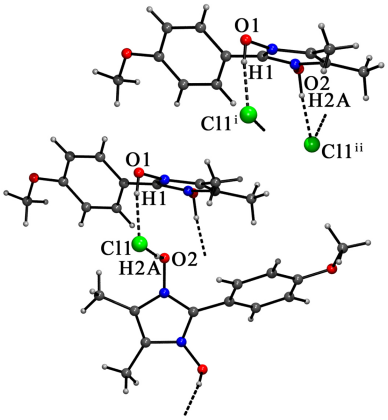

Figure 3. Interionic C–H···Cl interactions in DMPDI.

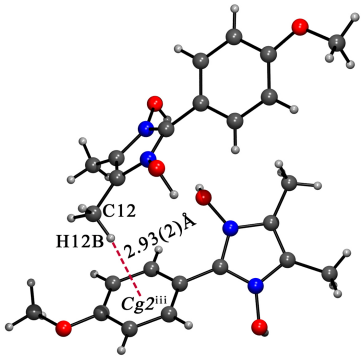

Figure 4. C–H···Cg interaction in the cationic unit of DMPDI.

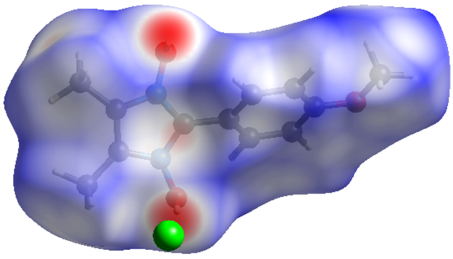

Figure 5. Hirshfeld surfaces plotted over the d_{norm} for the compound DMPDI.

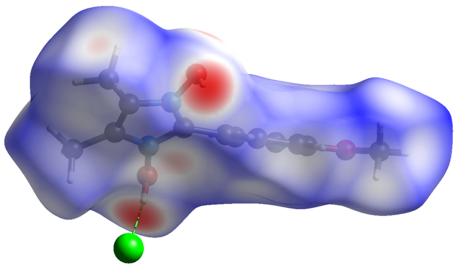

Figure 6. Hirshfeld surfaces plotted over the d_{norm} showing hydrogen bonding interaction.

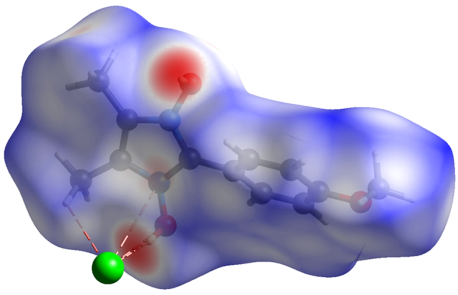

Figure 7. Hirshfeld surfaces plotted over the d_{norm} showing other significant interactions.

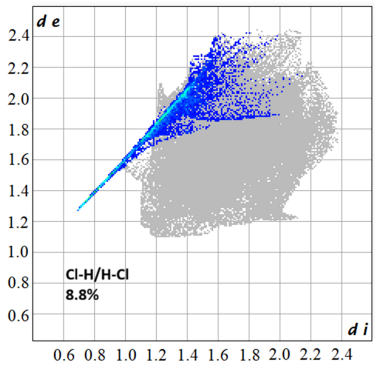

Figure 8. 2-D fingerprint plots showing Cl-H/H-Cl.

A closer visualization of the Hirshfeld surface analysis reveals several intermolecular contacts, *viz.*, N···Cl$^-$ contacts associated with imidazole and C-H···Cl$^-$ contacts involving the methyl group attached to the imidazole ring. Along with these, O-H···Cl$^-$ hydrogen bonding interaction involving the OH group attached to the imidazole nitrogen is observed (Figure 6). As is apparent, all close intermolecular contacts in the crystal packing are mediated by Cl$^-$ anions. All these interactions are visualized in Figure 7.

To obtain more detailed information on the intermolecular interactions, a 2D fingerprint plot is shown in Figures 8-11, where the contributions of the individual H-C/C-H, H-H, H-O to the total interactions have been shown. The C···H and H···H interactions are associated with 16.7 and 51.0% surface area, respectively, the H-O/O-H interactions are found to be 13.6%, the O-C/C-O interactions are found to be 4.0 % while the Cl-H/H-Cl interactions are found to be 8.8 %. Although the contributions of the Cl···H (8.8%) and O···H (13.6%) interactions are smaller, yet they are significant for the crystal architecture.

3.4. Quantum chemical calculation

To study the geometry and electronic transitions, density functional theory (DFT) studies of the title compound were also carried out. The structure optimization using the DFT method serves as a good alternative to ascertain different geometrical parameters. These geometrical parameters can then also be compared to those obtained from the X-ray single crystal structure of the compound. Thus, the geometrical parameters of the title compound DMPDI were optimized with DFT using Gaussian 16, Revision A.03 programme package within the framework of B3LYP/6-31G+(d,p).

3.5. Optimization of molecular geometry

The crystal structure and the optimized gas phase molecular geometry of the compound DMPDI with an atom labelling scheme are shown in Figures 12 and 13, respectively.

Geometrical parameters, such as bond lengths, bond angles, and torsion angles, are listed in Table 2. The theoretical C-H bond length for the phenyl ring was found in the range between 1.083 and 1.084 Å, and the experimental value was observed between 0.929(3)-0.955(3) Å. This larger difference between theoretical and experimental C-H bond length arises from the poor scattering coefficients of hydrogen atoms on X-ray diffraction studies [45] and from the fact that X-ray diffraction locates electron density rather than nuclear positions.

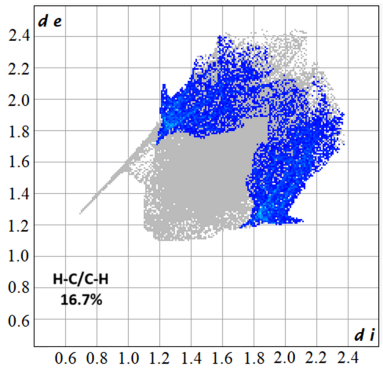

Figure 9. 2-D fingerprint plots showing H-C/C-H.

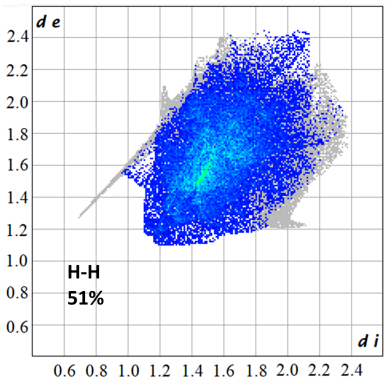

Figure 10. 2-D fingerprint plots showing H-H.

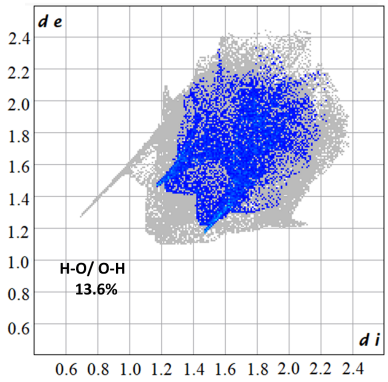

Figure 11. 2-D fingerprint plots showing H-O/O-H.

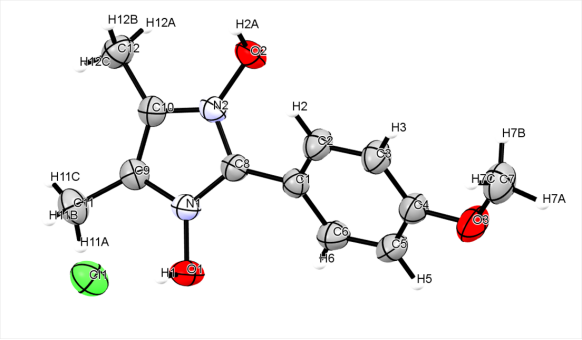

Figure 12. ORTEP diagram of DMPDI with atom labelling scheme.

Table 5. Comparison of notable bond lengths and torsion angles (Å, °) for the title compound.

	Experimental (X-ray)	DFT Optimized
N1-O1	1.3798 (18)	1.3747
N2-O2	1.3716 (18)	1.3723
C1- C8	1.460 (2)	1.4479
C9-C10	1.356 (2)	1.3680
N(1)–C(8)–C(1)–C(6)	46.1(3)	31.111
N(2)–C(8)–C(1)–C(2)	42.9(3)	31.310

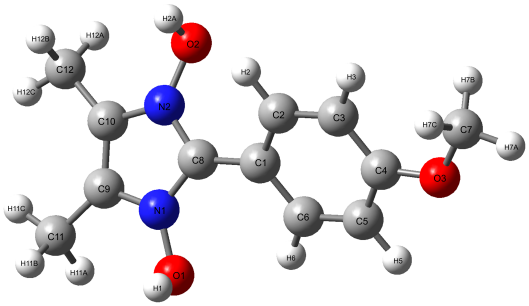

Figure 13. Optimized gas phase molecular geometry of DMPDI.

In C-H bonds, the electron density in hydrogen atom is not generally located near the atomic nucleus, but it is actually shifted toward the bonded carbon atom. As a consequence, C-H bond lengths obtained from X-ray diffraction are shorter than their true values, even in high-precision experiments [46]. The theoretical C-C bond length of the phenyl ring lies in the range 1.380-1.416 Å, which is in good agreement with the experimentally observed C-C bond length in the 1.380(3)-1.394(2) Å. These C-C bond length values are between the C-C single bond (1.54 Å) and C=C double bond (1.33 Å). The C1-C6 bond length observed at 1.416 Å (DFT) and 1.394(2) Å (experimental) is large due to the presence of the imidazole ring. The C-O bond lengths for C4-O3 = 1.341 Å (DFT) and C7-O3 = 1.432 Å (DFT) are in good agreement with the experimental values of 1.361(2) and 1.429(3) Å, respectively. For the imidazole ring, the theoretical C-N bond lengths for C8-N2, C8-N1, C10-N2, and C9-N1 observed at 1.358, 1.357, 1.396, and 1.394 Å, respectively, are in good agreement with experimental values of 1.34(2), 1.341(2), 1.378(2), and 1.383(2) Å. These C-N bond lengths are shorter than the value in the literature (1.48 Å). This may be attributed to the effect of resonance, difference of hybridization, and positive charge on a nitrogen atom of the imidazole ring. The theoretical C-C bond length for C10-C12 (1.489 Å) and C9-C11 (1.49 Å) is in good agreement with the experimentally observed values of 1.487(3) Å and 1.483(3) Å. The large values of these bond lengths can be attributed to the presence of methyl groups.

For the title compound, it is clearly seen that the dihedral angles for C1-C6-C8-N2, C1-C2-C8-N1 are observed at -148.08° (DFT), -135.93(2)° (experimental) and -148.88° (DFT), -135.06(19)° (experimental), respectively, indicates that the imidazole ring and the phenyl ring are not planar to each other. This is also supported by the torsion angle value for C2-C1-C8-N2 = 31.30°(DFT), 42.88(3)° (experimental), and C6-C1-C8-N1 = 31.72° (DFT), 46.12(3)° (experimental) [47].

The theoretical bond angles of the phenyl ring C5-C6-C1, C4-C5-C6, C4-C3-C2, and C2-C1-C6 were found at 120.44°, 120.56°, 119.76°, and 118.58°, respectively, which are in close agreement with experimental values of 119.99(19)°, 120.64(18)°, 119.48(19)°, and 118.92(17)°. For the imidazole ring, the bond angles N1-C8-N2 = 102.72° (DFT), 103.37(14)° (experimental) and C9-C10-N2 = 105.74° (DFT), 105.69(15)° (experimental) are in good agreement with each other.

The optimized bond lengths are in agreement with those observed in the crystal structure within the range of 0.02 Å (Table 5). However, there is a large distinction between the calculated and crystallographic geometries as seen in the difference of 11-15° in the torsional angle values, which is related to the twist of the anisole group attached to the carbon-2 of the imidazole ring system (Table 5). This could be due to hydrogen bonding and the hydrogen-bonding and C–H···C_g interaction.

3.6. Frontier molecular orbitals

The highest-occupied molecular orbital (HOMO) and the lowest unoccupied molecular orbital (LUMO) constitute the frontier molecular orbitals. HOMO is the higher-energy orbital containing the outermost electron, and, therefore, acts as an electron donor while LUMO is the lowest-energy orbital that has vacant space to accept electrons and, thus, acts as an electron acceptor. Frontier molecular orbitals are, therefore, essential quantum mechanical parameters that determine molecular reactivity, as the reactive properties in the case of organic molecules are primarily dictated by frontier molecular orbitals [26]. Their energy levels help to predict excitation properties and electron transport quantitatively [48,49]. The energies of the HOMO and LUMO orbitals of the compound DMPDI are calculated with the DFT/B3LYP method using the 6-31G+(d,2p) level of basis set and visualized in Figure 14. The areas where HOMO is localized designate molecule sites that could donate electrons, while areas where LUMO is localized designate molecule sites that could accept electrons.

The energy of HOMO and LUMO orbitals of the title compound is listed in Table 6. It is quite evident that the energy of the HOMO and LUMO orbitals for the compound is negative, inferring that the compound is relatively stable [50]. Interestingly, using the HOMO-LUMO energy, it is possible to calculate global chemical descriptors such as chemical potential, global hardness and global electrophilicity, which in turn are very helpful to understand the structure of molecule and its reactivity [51]. These new chemical descriptors could, in turn, help us understand the various aspects of the pharmacological properties of the molecule for the drug design process [52].

The ionization energy (I) and electron affinity (A) can be expressed in terms of HOMO and LUMO orbital energies as follows (Equation 4);

$$\mathrm{I} = -E_{\mathrm{HOMO}} \text{ and } \mathrm{A} = -E_{\mathrm{LUMO}} \quad (4)$$

Table 6. Energies of HOMO and LUMO orbitals, ionization energy (I), electron affinity (A), chemical potential (μ), electronegativity (χ), global hardness (η) and global electrophilicity power (ω) of DMPDI.

Parameters (eV)	DMPDI
E_{HOMO}	-9.25
E_{LUMO}	-4.94
ΔE	4.31
Ionization energy (I)	9.25
Electron affinity (A)	4.94
Chemical potential (μ)	-7.095
Electronegativity (χ)	7.095
Global hardness(η)	2.155
Electrophilicity power(ω)	11.68
Maximum charge transfer index (ΔN_{max})	3.29

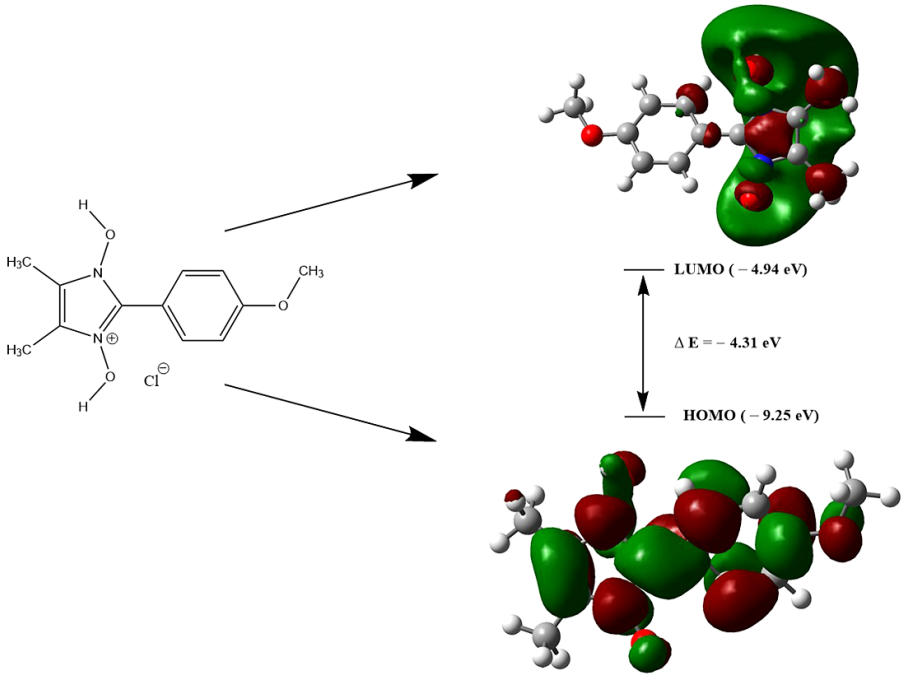

Figure 14. Energies of the HOMO and LUMO orbitals of DMPDI.

Chemical reactivity descriptors such as chemical potential (μ), electronegativity (χ), global hardness (η), and global electrophilicity power (ω) can be calculated with the help of the following relations (Equations 5-9);

$$\text{Chemical potential } (\mu) = \frac{E_{HOMO} + E_{LUMO}}{2} = -\frac{(I-A)}{2} \quad (5)$$

$$\text{Electronegativity } (\chi) = \frac{(I+A)}{2} \quad (6)$$

$$\text{Global Hardness } (\eta) = \frac{(-E_{HOMO} + E_{LUMO})}{2} = \frac{(I-A)}{2} \quad (7)$$

$$\text{Electrophilicity power } (\omega) = \frac{\mu^2}{2\eta} \quad (8)$$

$$\text{Maximum charge transfer index } (\Delta N_{max}) = \frac{-\mu}{\eta} \quad (9)$$

where I and A are the first ionization potential and electron affinity of the chemical species. The ionization energy (I), electron affinity (A), chemical potential (μ), electronegativity (χ), Global hardness (η), and global electrophilicity power (ω) of the title compounds are listed in Table 6.

The calculated chemical potential of the studied molecule is negative, suggesting that it does not decompose spontaneously into its constituent elements. Furthermore, the compound DMPDI has a HOMO-LUMO gap of 4.31 eV. Although relatively large, it is comparable to several reported bioactive and drug-like molecules. For example, HOMO-LUMO gaps of 4.13 eV for natural isoflavone biochanin-A [53], 3.9726 eV for 3,4-difluoroacetophenone thiosemicarbazone [54], and 6.113, 5.290 and 4.017 eV have been reported for anticancer drugs such as anastrozole, letrozole and tucatinib, respectively [55]. Although the HOMO-LUMO gap alone is not sufficient to describe the biological activity of the molecule, the observed HOMO-LUMO gap value lies within the range reported for stable bioactive or drug-like molecules. Furthermore, according to the conceptual DFT, hard molecules have a large HOMO-LUMO gap, while soft molecules have smaller gaps [56]. Global hardness signifies the resistance towards the deformation of the electron cloud of chemical systems under small perturbations that occur during the chemical reaction. Thus, a hard system is less polarizable than a relatively soft system [57]. Consequently, the relatively large energy gap of DMPDI indicates a higher global hardness. This relatively high global hardness indicates enhanced electronic stability and controlled reactivity, which may add to the ability of the molecule for selective biological interactions. As is evident from Table 6, the electrophilicity index of 11.68 eV for DMPDI indicates its electrophilic nature and has a high capacity to take electrons. The global electrophilicity power measures the stabilization of energy when the system acquires an additional electronic charge from the environment [58]. DMPDI's capacity to accept electrons easily may enhance its interaction with target protein molecules.

Table 7. Detailed description of MEP surface for DMPDI.

Entry	Negative region (red, orange, yellow)/ Electrophilic reaction site	Positive region (blue)/ Nucleophilic reaction site
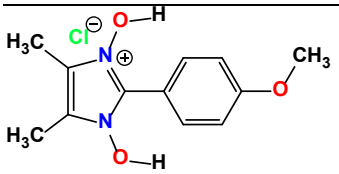	Electrophilic site toward the phenyl ring	Two =N-OH groups of the imidazole ring separately

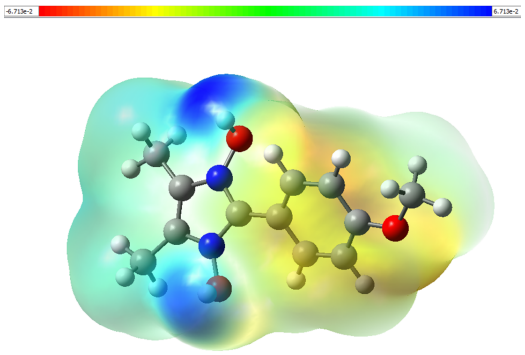

Figure 15. MEP plot of DMPDI.

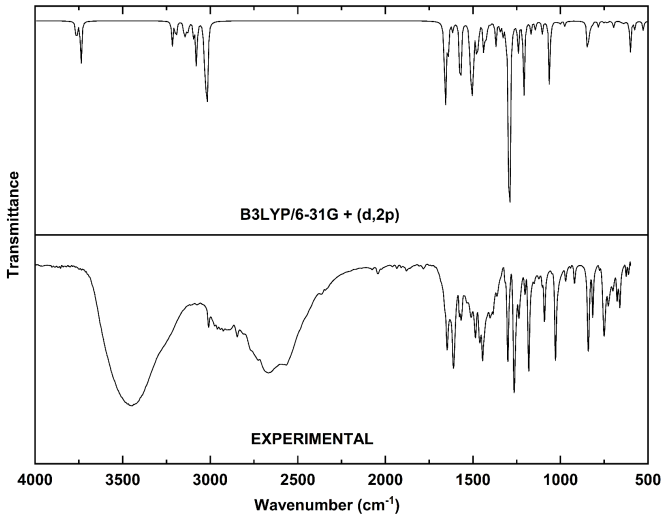

Figure 16. Theoretical and experimental FT-IR spectra of DMPDI.

3.7. Molecular electrostatic potential (MEP)

A chemical system always creates an electrostatic potential around itself, and the molecular electrostatic potential (MEP) is an important parameter for ascertaining and correlated between the molecular structure and the physicochemical properties of molecules [59]. MEP is also useful for understanding the sites of electrophilic and nucleophilic reactions, together with hydrogen-bonding interactions [60]. To predict the reactive sites of electrophilic and nucleophilic attack for the title molecule (DMPDI), MEP at B3LYP/6-31G+(d,2p) optimized geometry was calculated. Figure 15 provides a visual presentation of the MEP surface of the title compound (DMPDI). The most negative electrostatic potential (red, orange, and yellow regions) on the surface of the MEP is assigned for the electrophilic reaction sites, and the positive (blue region) corresponds to the nucleophilic reaction site [59,60].

From the MEP of the title compound, it is evident that the negative electrostatic potential (yellow/red/orange region) is located over the phenyl ring in the molecule, indicating the electron-rich region that is susceptible to electrophilic attack. While the presence of a positive electrostatic potential (blue region) over the OH group is apparent, it represents electron-deficient sites that are susceptible to nucleophilic reaction site attack. A detailed description of the MEP surface, indicating the region of negative/electrophilic reaction sites and positive/ nucleophilic reaction sites for the compound, is listed in Table 7.

3.8. FT-IR and Raman spectra analysis

The study of molecular vibrations of organic compounds has become an important area of interest for both experimental and theoretical chemists. The DFT method provides an avenue for the theoretical calculation of molecular vibrations of the studied system, and therefore, it is possible to correlate the

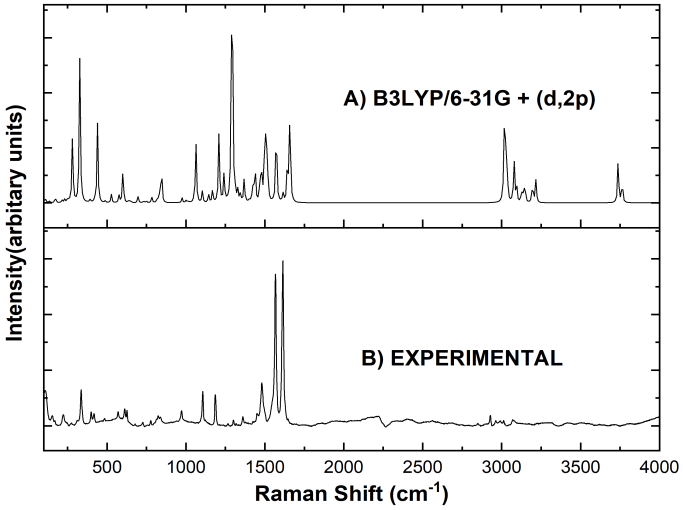

Figure 17. Raman spectra of DMPDI (A) theoretical (DFT) and experimental (B).

experimental and theoretical FT-IR and Raman spectra of the studied compounds to determine the different types of structural characteristics in the molecules [51]. Thus, the infrared and Raman vibrational spectra of DMPDI simulated using DFT at the B3LYP/6-31G+(d,2p) level of theory on the optimized geometry of molecules in the gas phase is scaled and compared with the experimental spectra (Figures 16 and 17) and the detailed vibrational assignments are discussed below and presented in ESI Table S1.

3.9. Vibrational assignments

3.9.1. CH_3 modes

In aromatic methoxy compounds, methyl stretching vibrations are expected in the region 3010-2900 cm^{-1} (asymmetric) and 2950-2850 cm^{-1} (symmetric) [61]. In the case of DMPDI, theoretically, methyl stretching vibrations were observed in the range 3147-3015 cm^{-1}, and the experimental IR bands are observed at 3009, 2959, 2941, 2925, and 2845 cm^{-1} and in the Raman spectrum at 3012, 2991, 2964, 2928, and 2849 cm^{-1}. The deformation modes for the methyl group [61] were observed at 1264, 1091 cm^{-1} in the experimental IR spectrum and at 1265, 972 cm^{-1} in the Raman spectrum, which is in good agreement with the theoretically calculated values in the range of 1498-974 cm^{-1}.

3.9.2. O-H modes

The literature concordant values for O-H stretching vibrations are generally expected to appear in the range of 3380±200 cm^{-1} [61]. Experimentally, the stretching vibration for the -OH group in the IR appeared at 3448 cm^{-1} as a broad and strong peak, and theoretically the -OH stretching vibrations were found at 3764 and 3738 cm^{-1}, and these values are assigned for the two -OH groups in the compound studied. The review revealed that the -OH stretching vibrations were found at 3661 cm^{-1} both experimentally and theoretically for similar compounds [62]. The literature value for the in-plane O-H deformation band is expected at 1440±40 cm^{-1} [61]. Theoretically, the in-plane O-H deformation band for the titled compound appeared at 1369.32 cm-1 and experimentally it was observed as a sharp peak at 1362 cm^{-1}. The literature review revealed -OH in-plane deformation peaks at 1318 cm^{-1} [63] and 1345 cm^{-1} [64]. However, discrepancies between the experimental and theoretical Raman bands for -OH vibrations were observed, and this can be ascribed to intermolecular interactions that are overlooked by the general scale factors in DFT calculations [65].

3.9.3. C-O modes

According to Varghese *et al.* [64], C–O stretching is observed at 1255 cm^{-1} in both IR and Raman spectra and theoretically at 1262 cm^{-1}. Experimentally, the IR C–O stretching frequency of the compound studied appeared at 1301 cm^{-1} as a sharp medium peak, which is inconsistent with the theoretically predicted value of 1291 cm^{-1}. This theoretically predicted vibrational band is a combination of the stretching vibration of the C-O bond of the phenyl ring, as well as the C-O stretching frequency of the methoxy group [66-68]. Similarly, the band observed at 1302 cm^{-1} in the Raman spectrum was assigned as C–O stretching vibrations.

3.9.4. N-O, C=N, and C-N modes

The review revealed that the identification and assignment of N-O stretching frequencies is usually difficult and inaccurate, especially in the case of compounds that have an N-O functional group such as nitrones, nitronates and nitrile oxides [69,70]. Similar compounds containing the nitroxide radical show that the N-O stretching mode lies between 1340 and 1380 cm^{-1} or near 1350 cm^{-1} [71,72], while other data show the vibrations between 1310 cm^{-1} for 3-carbamoyl-2,2,5,5-tetramethyl-3-pyrrolin-1-yloxyl and 1370 cm^{-1} for tert-butyl-phenyl nitroxide [71,73]. Thus, the accepted band position of the N-O stretch is less than N=O (1600-1500 cm^{-1}) [74] but greater than the N-O stretch in oximes (965-930 cm^{-1}) [75] due to its bond and half character [76]. Previously, Rintoul *et al.* [77] have reported a N-O stretch at 1428 cm^{-1} (IR), 1431 cm^{-1}(Raman) and 1433 cm^{-1} (DFT).

Theoretically, the N-O stretching modes for DMPDI were observed in the range 1402–1468 cm^{-1} due to a mixture of contributions from different modes, with 1438 cm^{-1} having the highest contribution from the N-O stretching mode. Experimentally, the FT-IR spectrum provides inverse M-shaped sharp bands corresponding to 1444, 1460, and 1486 cm^{-1}, while sharp bands at 1480 cm^{-1}, along with two other weaker bands at 1450, 1423 cm^{-1} in the Raman spectrum, are observed.

The C=N stretching modes are reported at 1592 cm^{-1} (IR) [78] and 1535-1666 cm^{-1} (IR) [79], with a theoretically reported value of 1584 cm^{-1} [78]. For the compound studied, the

theoretical stretching mode C = N was found at 1658 cm^{-1} with mixed contributions from other stretching modes such as C-N and C=C-C=C in the phenyl ring. In the Raman spectrum, a sharp peak at 1566 cm^{-1} was observed and was assigned to C=N stretching modes, which is in good agreement with the literature [78,79]. A sharp peak for the C=N vibration is seen in the IR spectrum at 1611 cm^{-1} with a complementary weaker but sharp doublet peak at 1647 cm^{-1}. This has been attributed to the presence of strong resonance due to the formal charge in the imidazole ring, and can be compared to the work on poly (ionic liquids) reported by Alessandro Dani *et al.* [80].

Rings with nitrogen present directly on the ring have been reported to absorb strongly in the range 1260-1330 cm^{-1} due to the stretch of the phenyl C-N bond [80]. For the compound studied, C-N vibrations are assigned to 1241, 1168, and 974 cm^{-1} theoretically, while C-N vibrations are assigned to 1264, 1181, and 970 cm^{-1} in the experimental IR spectrum and 1265 and 1185 cm^{-1} in the Raman spectrum. The theoretical values are in good agreement with the experimental values and those of the literature [81,82].

3.9.5. C=C and C-C vibrations

C=C stretching vibrations have been reported to be present in the spectral region of 1650-1430 cm^{-1} [83] or 1600±50 cm^{-1} [84]. In the compound studied, the imidazole ring C=C bond stretch is observed at 1611 cm^{-1} in IR with contribution from C=N vibration as well and a strong, sharp peak at 1614 cm^{-1} in Raman, while theoretically it was found at 1642 cm^{-1}. The C=C theoretical stretching vibrations have previously been reported at 1625 cm^{-1} [85]. Experimentally, C-C stretching vibration can be attributed to the values 1384, 1362, 1181, 1091, 1028 cm^{-1}in IR and to 1359, 1106 cm^{-1} in Raman, with some mixing with other stretching modes. Theoretically, these vibrations were found in the range 1369-974 cm^{-1}.

3.9.6. Phenyl ring modes

Benzene rings have been known to possess six ring stretching vibrations, and four of them with the highest wave numbers are good group vibrations (occur near 1600, 1580, 1490, and 1440 cm^{-1}). For the compound DMPDI, the bands for phenyl stretching rings are observed at 1647, 1611, 1577, 1567, 1509, 1486 cm^{-1} in the IR, 1650, 1597,1450, 1425 cm^{-1} in the Raman spectrum, and at 1658, 1642, 1614, 1571, 1514 cm^{-1} theoretically. The expected range for these modes is 1620-1250 cm^{-1} [62]. The sixth ring stretch vibration (or ring breathing mode) can appear as a weak band near 1000 cm^{-1} for mono, 1,3-disubstituted, and 1,3,5-trisubstituted benzenes. In other cases, this vibration mode is sensitive to the substituent and difficult to distinguish from ring in-plane deformations [73]. Thus, the ring breathing modes for *para*-substituted benzenes with completely different substituents are reported to be strongly IR active, with most of their bands present in the region interval of 840-740 cm^{-1} [72]. For DMPDI, the ring breathing mode is assigned to 783 cm^{-1} theoretically and observed at 750 cm^{-1} as a strong and sharp peak in the IR spectrum and is consistent with literature [86].

The C-H stretching modes for the aromatic ring are commonly exhibited as multiple weak bands that occur in the range of 3100-3000 cm^{-1} [61]. For DMPDI, weak bands are observed at 3080, 3009, 2959 cm^{-1} in the IR, and 3177, 3069, 2890 cm^{-1} in the Raman spectrum, while theoretically the C-H stretching modes were assigned to 3218, 3215, 3198, 3191 cm^{-1}. For *para*-substituted benzenes, the δC-H modes are seen in the range of 1315-990 cm^{-1} [62]. For the phenyl ring, the band observed at 1091 cm^{-1} in the IR spectrum is assigned to the δC-H mode and is theoretically seen at 1209, 1143, 1065, 1026 cm^{-1}.

Out-of-plane C-H deformations are seen in the range of 1000-700 cm^{-1} [61]. In general, C-H out-of-plane deformations with lower wavenumbers are seen to have higher intensities than those absorbing at higher wavenumbers. Thus, a very strong C-H out-of-plane deformation band typically occurs at 840±50 cm^{-1} for 1,4-disubstituted benzenes [61,73]. For DMPDI, a very strong, sharp peak is seen at 841 cm^{-1} in the IR spectrum and is therefore assigned to the γC-H mode. The theoretical calculation gives this value at 948, 844, and 819 cm^{-1}. The theoretical mode, which is most consistent with the experimental value, is 844 cm^{-1} and is consistent with the literature [61,87]. K.B. Benzon *et al.* [26] reported that the C-H deformation bands at 933, 932, 803, 786 cm^{-1} in Raman, thus the peaks at 837, 823, 776 cm^{-1} are assigned for the same.

3.9.7. Hydrochloride salt modes

The product DMPDI was obtained as a solid and was suspected to be a hydrochloride salt of the N-oxide compound. This observation was partially confirmed due to the presence of stretching frequencies at 2667 and 2565 cm^{-1} in the IR spectrum, which is consistent with previous work done by J.B. Wright [88]. However, these frequencies are not reproduced in the theoretical IR-spectrum because the calculations were done in the gas phase for the isolated cation and do not explicitly include the chloride counterion or ion-pair interactions. Proper reproduction of the salt- specific modes would require explicit modeling of the cation-anion pair, which was beyond the scope of the present gas-phase DFT calculations. However, the remaining calculated and experimental FT-IR data show good agreement. Further investigations need to be carried out with a focus on ion pair modeling using implicit solvent to reproduce these modes accurately and totally confirm the hydrochloride salt modes.

3.10. Hyperpolarizability (NLO properties)

Non-linear optical properties are expressed in materials under the influence of applied electromagnetic fields, which causes the generation of new electromagnetic fields with a change in phase, wavenumber, or other physical properties [89]. Organic molecules that proficiently manipulate photonic signals play a vital role in the progression of technologies like optical communication and optical computing. These molecules facilitate faster data transmission, enhance efficiency in signal modulation efficiency, and contribute to the development of more compact devices. As the demand for faster and more efficient computing systems continues to increase, the significance of organic molecules in these domains becomes increasingly pronounced. Furthermore, their application in dynamic image processing can significantly improve fields such as medical imaging and particle analysis by boosting image resolution and processing speed [90-92].

The dipole moment (μ), polarizability (α), first-order hyperpolarizability (β), and second-order hyperpolarizability (γ) can be calculated from the output of Gaussian software used to optimize the compound DMPDI theoretically. The calculations are based on the finite-field approach, i.e., the energy of a system is a function of the applied electric field on it. Kleinman symmetry is used to reduce the 27 components of the 3D matrix describing a system, to a simplified 10 component system [93]. The Taylor series expansion of the energy of a system in an external electric field gives the components as the coefficients μ, α, β, and γ. When the electric field is homogeneous and weak, the expansion is expressed as (Equation 10),

Table 8. Experimental and calculated ^{1}H NMR parameters (with respect to TMS).

Protons	σ_{TMS}	B3LYP/6-311+G(d,2p) (σ_{calc})	$\delta_{calc} = \sigma_{TMS} - \sigma_{calc}$	Exp. δ_{ppm}
H6	31.8821	24.8352	7.0468	7.94
H5		25.4844	6.3976	7.92
H3		25.6793	6.2027	7.20
H2		25.7514	6.1306	7.18
H2a		27.2422	4.6398	13.51
H1		27.3755	4.5065	13.51
H7a		27.8897	3.9923	3.86
H7b		28.0884	3.7936	3.86
H7c		28.1075	3.7745	3.86
H12a		29.3807	2.5013	2.26
H11a		29.5033	2.3787	2.26
H12c		29.6855	2.1965	2.26
H11c		29.7550	2.1270	2.26
H11b		29.7695	2.1125	2.26
H12b		29.8784	2.0036	2.26

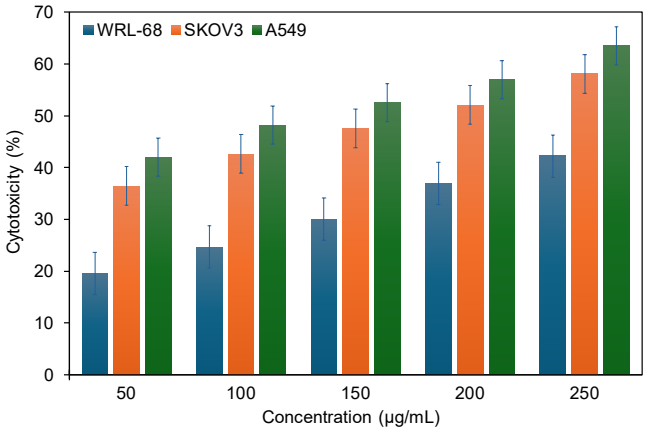

Figure 18. Comparison of the percentage cytotoxicity of DMPDI in A549, SKOV3 and WRL-68 cell lines.

$$E = E_0 - \sum_i \mu_i F^i - \frac{1}{2}\sum_{ij} \alpha_{ij} F^i F^j - \frac{1}{6}\sum_{ijk} \beta_{ijk} F^i F^j F^k - \frac{1}{24}\sum_{ijkl} \gamma_{ijkl} F^i F^j F^k F^l + \ldots. \quad (10)$$

where E_0 is the energy of the unperturbed molecule, F^i is the field at the origin point, μ_i, α_{ij}, β_{ijk}, γ_{ijkl} are the components of dipole moment, polarizability, first hyperpolarizability, and second hyperpolarizability, respectively [94].

The calculated first hyperpolarizability of DMPDI is 0.606 × 10-30 esu, which is 4.52 times that of the standard urea (0.134×10^{-30} esu) [95]. The average second hyperpolarizability is $< \gamma >= 1/5\ (\gamma_{xxxx} + \gamma_{yyyy} + \gamma_{zzzz} + 2(\gamma_{xxyy} + \gamma_{yyzz} + \gamma_{xxzz}))$. The calculated second-order hyperpolarizability for DMPDI is -1.123×10^{-36} esu, while the dipole moment, polarizability, and anisotropy of polarization are calculated as 5.39 Debye, -13.836×10^{-24} esu, and 2.585×10^{-24} esu. The comparison of these values with that of urea is given in the ESI (Table S2). It is thus concluded that the studied compound can be further studied for its nonlinear optical properties.

3.11. ^{1}H NMR spectrum

The experimental ^{1}H NMR spectrum data of the compound DMPDI were obtained at 500 MHz in DMSO-d_6, taking TMS as an internal standard, and compared with theoretical analysis (Table 8). In addition to the diagnostic IR peak region (between 2500 and 2700 cm^{-1}) for the Imidazolium salts, as already mentioned, we found that the NMR spectra could also be used to provide additional information to characterize the salts. It is observed that the proton signal for the 1-hydroxyl group of a 1-hydroxy imidazole-3-oxide may be conspicuously present or absent, depending on the concentration of the sample used for the analysis. Although intriguing, it has been mentioned that these types of compounds form association complexes by extremely strong hydrogen bonds, and their ^{1}H NMR spectra are therefore dependent on the concentration [96]. This is also because the charge on both nitrogen atoms of the imidazole ring is the same, and the N-OH proton moves rapidly with respect to the NMR time scan [26]. However, the proton peaks of the hydroxyl groups are always found in the ^{1}H NMR spectra of the 1,3-dihydroxy imidazolium salts. This may be because there is no scope anymore for N-hydroxy protons to shuttle. The charge on both nitrogen atoms of the imidazole ring is still equal, as the NMR spectra of the 1,3-dihydroxy imidazolium salts show that the two methyl groups at 4,5 positions of the Imidazole ring are equivalent. The equivalency of charge on the nitrogen atoms is possibly caused by the shuttling of the chloride ion.

The observed chemical shift is in good agreement with the experimental ^{1}H data for methyl, methoxy, and phenyl hydrogens. The experimental chemical shift for the hydrogens of the hydroxyl group (H1, H2a = δ 13.51 ppm) does not match the theoretical values of δ 4.50 ppm (H1) and δ 4.63 ppm (H2a). This is because the theoretical calculations are run in the gas phase, where the molecule is not subject to hydrogen bonding effects.

3.12. Antiproliferative activity studies

A cell viability assay was performed taking the synthesized molecule, DMPDI, against human lung cancer cell line (A-549), human ovarian cancer (SKOV3), and human normal liver (WRL-68) cell lines. The results show that the compound DMPDI has obvious antiproliferative activity in the lung cancer A-549 as well as in the SKOV-3 ovarian cancer cell line, with IC_{50} values of 458.6 µM (124.18 µg/mL) and 645.7 µM (174.78 µg/mL),

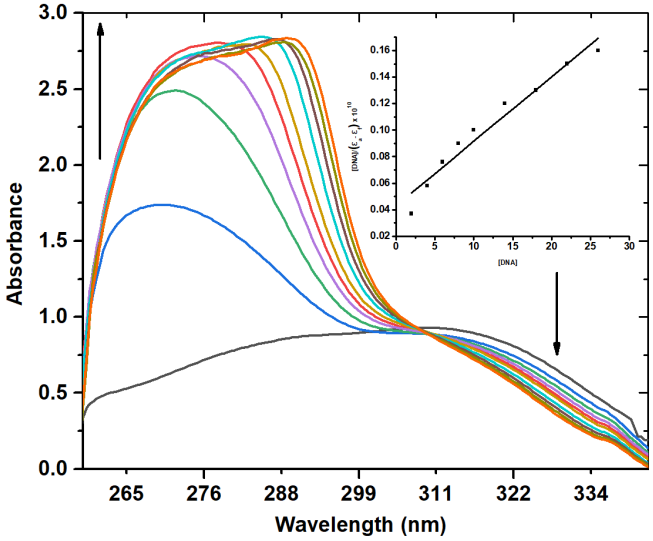

Figure 19. Absorption titration spectra of DMPDI in the absence (black line) and presence (other lines) of CT DNA to DMPDI at rt. The arrows indicate the absorbance change corresponding to an increasing CT DNA concentration. Inset: [DNA]/(ε_a-ε_f) vs [DNA] plot for the binding constant (K_b).

respectively, at 24 hours of treatment. The IC_{50} value of DMPDI was 1173 µM (317.49 µg/mL) against the WRL-68 cell line. The selectivity index of the compound was also calculated and was found to be 2.5 and 1.8 for A-549 and SKOV3, respectively. These values indicate only modest selectivity toward cancer cell lines. Although the compound shows a preference for cancer cells over normal cells, further structural optimization will be necessary to improve its therapeutic potential and selectivity. The results obtained are given in Figure 18. From this experiment, it was obvious that the DMPDI molecule has potent anticancer activity against both human lung and ovarian carcinoma, with a lower effect on normal cells.

3.13. DNA binding studies

DNA binding interactions are crucial for the anticancer activity of small molecules, particularly when these molecules target enzymes such as topoisomerase, which are involved in DNA processing. Small molecules that interact with DNA can fortify or weaken the DNA structure, directly affects the important biological processes such as replication and transcription [97]. Many anticancer drugs, such as anthracyclines and camptothecin, rely on these interactions to induce DNA damage or inhibit enzymes such as topoisomerases. This leads to cell cycle arrest and apoptosis [98]. The ability of small molecules to selectively target DNA grooves or intercalate between base pairs can enhance their therapeutic potential while minimizing off-target effects [99]. To study the interaction of DMPDI with DNA, we conducted UV-vis absorption titration and ethidium bromide (EB) displacement fluorescence assays using calf thymus DNA (ct-DNA) as a model system.

3.14. UV-vis absorption titration

The UV-vis absorption spectra of the compound in the absence and presence of increasing concentrations of CT-DNA are shown in Figure 19. The free compound exhibited a prominent absorption band centered around 260 and 315 nm, indicative of its aromatic π-conjugation. Upon incremental addition of CT-DNA, a small to moderate hypochromic effect with no significant blue or red shift for the band at 315 nm was observed. On the other hand, hyperchromism with a red shift was observed for the band at 260 nm. The nature of the absorption spectrum confirms that the compound interacts with the DNA and disturbs the electronic environment of the DNA-chromophore complex. The appearance of a distinct isosbestic point at 309.5 nm confirms the clean equilibrium between the free compound and the DNA-bound complex, consistent with a 1:1 binding stoichiometry [100]. It has been suggested that classical intercalators typically exhibit strong hypochromism along with a comparatively large red shift due to π-π stacking interactions between the intercalating molecule and DNA base pairs [101,102]. However, hyperchromism with a small or negligible shift in wavelength is often observed for groove binders [103,104]. In the present case, the absence of significant hypochromism and large wavelength shifts, together with the presence of pronounced hyperchromism at 260 nm with a slight red shift, suggests that the compound DMPDI interacts with CT-DNA predominantly through a non-intercalative, most likely groove-binding mechanism. Similar UV-vis spectral changes have been observed for other similar small organic molecules such as the benzimidazole Schiff base, which is found to exhibit hyperchromism at 250 nm and hypochromism at 390 nm and is interpreted as groove binding [100]. The intrinsic binding constant (K_b) calculated using the Wolfe–Shimmer equation was found to be 1.137×10^5 M^{-1}. This moderate binding constant value is also comparable to that of many small molecules that bind to grooves and is significantly lower than that of classical intercalators, which typically range in the order of 1×10^7 M^{-1} [105].

3.15. Ethidium bromide displacement assay

To further investigate binding affinity, an ethidium bromide (EB) displacement assay was conducted [106]. EB is a widely recognized intercalator of DNA, whose fluorescence intensity increases markedly upon intercalation into the DNA structure. The addition of a quencher to a DNA sequence displaces ethidium bromide (EB) and reduces the fluorescence intensity. This process forms the basis of the displacement method. The quenching occurs due to the decrease in the number of binding sites on the DNA available for EB decreases [43]. The emission spectra of the EB-DNA complex in the absence and presence of DMPDI are shown in Figure 20. As seen in the figure, with an increase in the concentration of DMPDI, the fluorescent intensity decreases compared to that of the initial measurement.

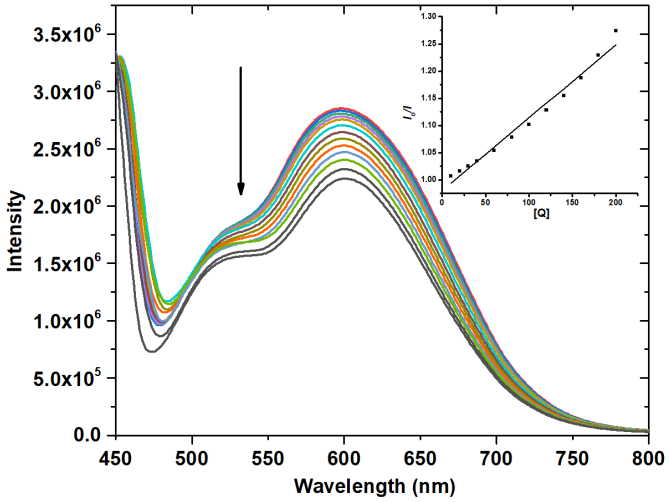

Figure 20. Emission spectra of EB bound to DNA (red line) and in the presence of DMPDI (other lines) with increasing amounts of 10-200 µL. The arrows indicate the change in emission intensity corresponding to an increase in the concentration of DMPDI. Inset: Stern-Volmer plot of the EtBr-DNA fluorescence titration.

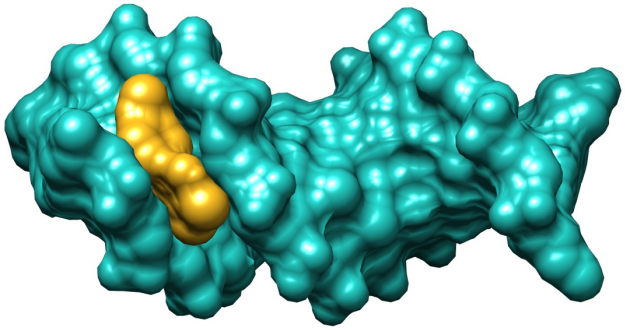

Figure 21. Surface view docking binding site visualization of the DNA (PDB ID: 1BNA) with DMPDI.

This observation supports the conclusion that DMPDI can remove EtBr from its DNA binding sites [107,108]. The value of the quenching constant (Ksv) determined from the slope of the plot of I_0/I vs [Q] based on the Stern-Volmer equation is $1.34(\pm0.2)\times10^3$ M^{-1}.

In summary, the combination of the analysis of UV-vis absorption and fluorescence results shows a strong affinity of DMPDI for ct-DNA, with groove binding emerging as the primary mechanism. The clearly defined isosbestic point and the recorded hypochromic/hyperchromic alterations emphasize the formation of a well-characterized 1:1 complex. Such DNA interactions are likely to contribute to the anticancer activity of the compound, together with its topoisomerase I inhibitory potential.

3.16. Molecular docking analysis with the B-DNA dodecamer (1BNA)

To complement the spectroscopic analyzes related to the DNA binding studies, a molecular docking study was performed to gain insight into the binding mechanism of the compound with the B-DNA dodecamer (PDB ID: 1BNA). The compound was adeptly docked into the DNA configuration, unveiling favorable binding interactions. The calculated binding energy was -7.2572 kcal/mol, indicating a reasonable affinity for the DNA duplex. This result is consistent with the moderate binding constant estimated from the UV-vis titration study (K_b = 1.137×10^5 M^{-1}). Analysis of the binding pose revealed that the compound engages with the DNA groove through a multifaceted combination of hydrogen bonding, π-π stacking, and carbon–hydrogen interactions. In particular, hydrogen bonds were formed with guanine bases at DG B:16 and DG A:10, both at a distance of 2.293 Å, as well as with DG B:14 at a distance of 2.618 Å, thus stabilizing the complex through direct interactions with DNA bases. A π-π T-shaped interaction was found with cytosine at position DC A:11 (5.830 Å), which contributes to overall stacking interactions and stabilization within the groove. Furthermore, a carbon–hydrogen bond with DG B:16 (3.005 Å) further increases the binding affinity of the compound. These interactions, along with the three-dimensional representation shown in Figures 21-23, basically imply that the compound primarily engages in groove binding, with localized stabilization facilitated by hydrogen bonding and π-π interactions.

A summary of the results of the docking study with corresponding binding affinity, interacting DNA bases, and type of interactions is presented in Table 9. This combined experimental and computational approach validates the DNA-binding capability of DMPDI and provides a structural basis for its interaction mode, which likely contributes to its observed anticancer activity.

3.17. Molecular docking analysis with human topoisomerase I (1RRJ)

Human DNA topoisomerase I (Topo I) was chosen as the molecular target for docking experiments because of its crucial function in relaxing supercoiled DNA during transcription, recombination, and replication. It is important to note that Topo I is often overexpressed in a variety of malignancies, such as

Table 9. Summary of docking of DMPDI against B-DNA dodecamer (PDB ID: 1BNA).

Compound	Binding energy (kcal/mol)	Residues /Atom	Type of interactions
DMPDI	-7.2572	DG16, DG10, DG14 and DC11	Hydrogen bonding, π-π-sigma, and carbon–hydrogen bonding

Table 10. Summary of the docking of DMPDI with the human topoisomerase I receptor protein (1RRJ)

Compound	Binding energy (kcal/mol)	Residues/Atom	Type of interactions
DMPDI	-7.9518	DG11, ARG364, DA113, DT10, ASP533, ILE535, HIS632, LYS532, PTR723, ARG488, DG12 and THR718	Hydrogen bonding, π–π-sigma, π–π stacking, π–π-anion, Alkyl, π- π-Alkyl, Carbon–Hydrogen bonding and van der Waals

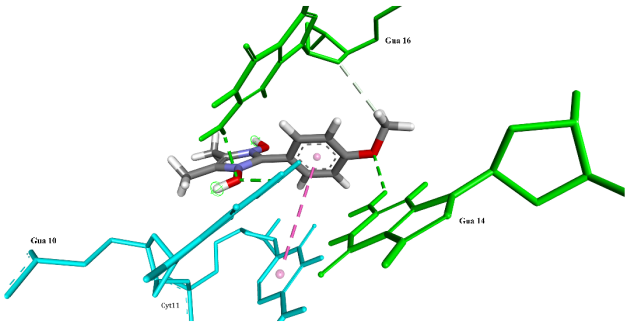

Figure 22. 3D interactions docking results visualization of the DNA (PDB ID: 1BNA) with DMPDI.

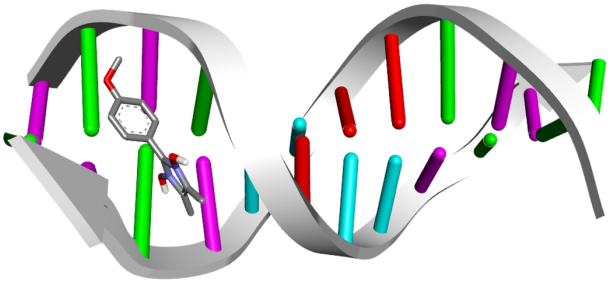

Figure 23. Ribbon view 3D docking results visualization of the DNA (PDB ID: 1BNA) with DMPDI.

ovarian cancer and lung cancer [109,110], where it aids in tumor growth by promoting rapid cell division and genomic stress adaptation Since Topo I is a confirmed target of several potent anticancer drugs, including camptothecin and its derivatives (*e.g.*, topotecan, irinotecan), it makes rationale for compounds exhibiting cytotoxicity against cancer cell lines to target this enzyme [111]. Furthermore, Topo I inhibition is a desirable target in precision oncology techniques because it can selectively cause DNA damage in tumor cells with impaired DNA repair mechanisms [112,113]. To assess the binding affinity and investigate the possible mechanism behind the observed anticancer effect of DMPDI, molecular docking against Human Topoisomerase I (PDB 1RRJ) was carried out.

DMPDI was docked into the binding pocket where the co-crystallized topotecan was present, and then the binding interactions were analysed. Multiple non-covalent interactions between the ligand and the 1RRJ protein were identified through the docking studies. The identification of a hydrogen bond between the ligand and the guanine residue DG B:11 of the DNA at a distance of 2.395 Å and two hydrogen bonds with arginine residue ARG A:364 of the protein at a distance of 2.463 and 2.515 Å, respectively, was suggestive of stabilization via base-specific and polar contacts. Furthermore, a π-π-sigma interaction was observed with DA C:113 at a distance of 3.570 Å and two more similar interactions with DG B:11 at a distance of 3.650 Å and 3.880 Å. Additionally, the ligand exhibited substantial π-electron interaction with nucleobase rings by forming π–π stacking interaction with DG B:11 (two interactions, distances: 4.350 Å, 4.17 Å), DT B:10 (distance: 4.630 Å), and DA C:113 (distance: 4.670 Å). A π-π-anion interaction was found with ASP A:533 at a distance of 3.920 Å, along with an alkyl interaction with ILE A:535 at a distance of 5.03 Å, and a π-π-alkyl interaction with HIS A:632 at a distance of 4.79 Å. The overall binding affinity of DMPDI and molecular stability was further enhanced by carbon–hydrogen bond interaction with ASP A:533 at a distance of 3.44 Å. Furthermore, van der Waals interaction with LYS A:532, PTR A:723, ARG A: 488, DG B:12, and THR A:718 were also observed. The binding energy of -7.9518 Kcal/mol was obtained as calculated by Autodock vina. All binding interactions discussed above are shown in Figures 24-26, with 2D and 3D interaction diagrams.

A detailed analysis of the docking result showed that the ligand binds to the protein with a binding affinity of -7.9518 kcal/mol. A summary of the results of the docking study with the corresponding binding affinity, interacting amino acid residues, and type of interactions is presented in Table 10.

3.18. In silico ADME prediction

In silico ADME (absorption, distribution, metabolism, excretion) profiling constitutes a pivotal phase in the preliminary stages of drug discovery, aimed at assessing the drug-like characteristics and pharmacokinetic properties of a candidate molecule. Assessment of ADME characteristics at an early stage is imperative to minimize the risk of attrition in the later stages of drug development.

Table 11. In silico ADME parameters for DMPDI.

MW (g/mol)	Fraction Csp^3	RB	HA	HD	TPSA	iLOGP	LogS	GI	Pgp	Lipinski violations	B Score
270.71	0.25	2	3	2	58.5	-4.03	-4.06	High	Yes	0	0.55

RB: Number of rotatable bonds, HA: number of H-bond acceptors, HD: number of H-bond donors, TPSA: topological polar surface area, iLOGP: partition coefficient between *n*-octanol and water ($logP_{o/w}$), LogS: molar solubility in water, GI: gastrointestinal absorption, Pgp: P-glycoprotein substrate, B Score: Bioavailability score.

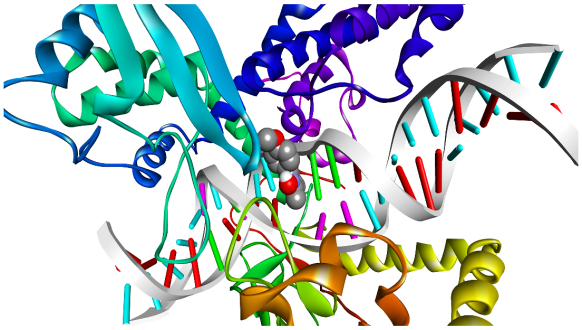

Figure 24. Visualization of the result of the binding site docking of DMPDI with human topoisomerase I (PDB ID: 1RRJ).

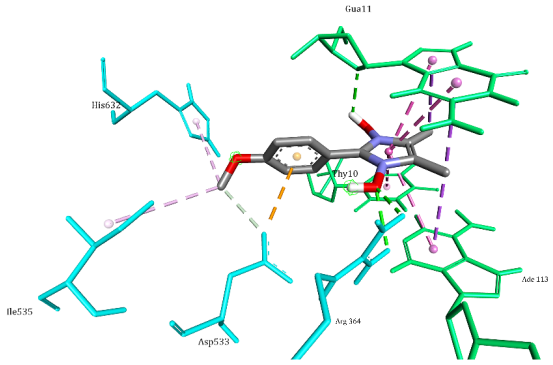

Figure 25. Visualization of the results of the 3D interaction coupling of DMPDI with human topoisomerase I (PDB ID: 1RRJ).

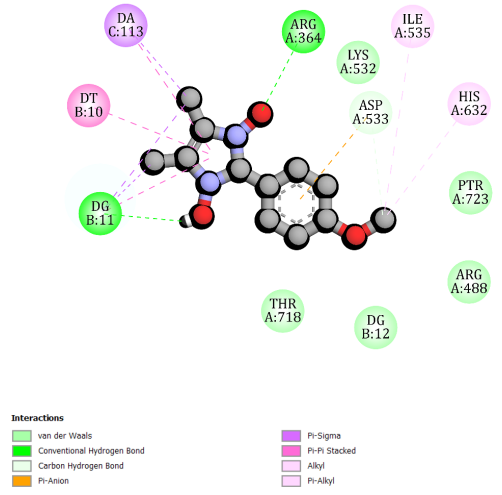

Figure 26. Visualization of docking results of DMPDI with human topoisomerase I (PDB ID: 1RRJ): 2D representation of amino acid residues and nucleotides involved in different interactions.

In the present investigation, the in silico ADME analysis of DMPDI was performed utilizing SwissADME (http://www.swissadme.ch/), a well-regarded online platform for the prediction of essential druglike properties [114]. Parameters such as molecular weight (MW), lipophilicity (iLOGP), topological polar surface area (TPSA), hydrogen bonding potential, number of rotatable bonds, and a range of drug-likeness criteria (Lipinski, Veber, Egan, Muegge), were obtained.

The investigation revealed favorable drug-likeness and oral bioavailability indicators. The compound has a molecular weight of 270.71 g/mol, a topological polar surface area (TPSA) of 58.5 Å^2, and no violation of Lipinski's, Veber's, Egan's, and Muegge's rules. The number of hydrogen bond donors (2), acceptors (3) and rotatable bonds (2) falls within the

established parameters conducive to optimal oral absorption [114]. Although the iLOGP value of –4.03 indicates a low degree of lipophilicity, which can adversely affect membrane permeability, this limitation could partially be mitigated by favorable hydrogen bonding interactions [115] and molecular flexibility [116]. However, the low lipophilicity should be considered as a key factor in further structural optimization of DMPDI derivatives in the context of drug development. The compound has a bioavailability score of 0.55, suggesting sufficient oral absorption [117]. Overall, these computational assessments complement our in vitro data, indicating that DMPDI represents a viable candidate for drug use [118]. The various ADME parameters discussed are listed in Table 11.

4. Conclusions

In conclusion, here we report the crystal structure of 1,3-dihydroxy-2-(4-methoxyphenyl)-4,5-dimethyl-1*H*-imidazol-3-ium chloride (DMPDI) together with its Hirshfeld analysis. The synthesized compound has been characterized by different analytical and spectroscopic techniques. DFT calculations were carried out to compare the geometry of the title compound with its crystal data. The calculated geometric parameters are found to agree well with those obtained experimentally. Analysis of the title compound has revealed various types of interactions that prevailing in the crystal structure. The FT-IR and Raman studies of the title compound in the ground state are reported experimentally and theoretically. Vibrational frequency assignments reveal a good match between the experimental and calculated values. Furthermore, it was found that the experimentally obtained vibration frequencies between 2500 and 2700 cm^{-1} in FTIR could be taken as diagnostic peaks for the 1,3-dihydroxy-2-(aryl)-4,5-dimethyl-1*H*-imidazol-3-ium chloride compounds. MEP predicts the most reactive part of the molecule. The MEP of DMPDI indicates that the negative potential site is on the phenyl ring, while the positive potential site is on the imidazole ring bearing the two hydroxy groups. The title compound may also serve as a good candidate for non-linear optical studies. Most significantly, *in vitro* studies of the compound with different cancer cell lines, A-549 lung cancer and SKOV-3 ovarian cancer cell lines, were carried out and the cytotoxicity of the compound was compared with the normal hepatic cell line WRL-68. Although the compound exhibits good anticancer activity, its selectivity indices (SI = 1.8-2.5) are still modest over normal cell lines, which is a primary limitation of the current compound. Future efforts will focus on structural modifications to enhance its SI and therapeutic potential. The antiproliferative activity findings are further supported by DNA binding studies. To complement spectroscopic analyses pertaining to DNA binding studies and *in vitro* cytotoxicity studies, molecular docking studies were also performed to gain insight into the binding mechanism of the compound with the B-DNA dodecamer (PDB ID: 1BNA) and the human topoisomerase I receptor protein (1RRJ). The computed binding energies were determined to be -7.2572 kcal/mol for the B-DNA dodecamer and -7.9518 kcal/mol for the human topoisomerase I receptor protein (1RRJ). It suggests that the title compound, after necessary derivatization and suitable functionalisation, could offer suitable candidates for the development of anticancer agents in the future.

Acknowledgements

The authors are grateful to the Department of Chemistry, Department of Biotechnology, University of North Bengal and Incubation Centre, St. Joseph's College Darjeeling, for providing the infrastructural and analytical facilities. The authors thank Sudarshan Pradhan for his valuable assistance in conducting the DNA binding studies. The authors, Munna Mukhia and Sumiran Tamang, are thankful to the state government for the Swami Vivekananda Merit-cum-Means Scholarship and the Council of Scientific and Industrial Research, New Delhi, for a fellowship (09/0285(13198)/2022-EMR-I), respectively.

Supporting information

CCDC-2183509 contains the supplementary crystallographic data for this paper. These data can be obtained free of charge via https://www.ccdc.cam.ac.uk/data-request/cif, or from Cambridge Crystallographic Data Centre, 12 Union Road, Cambridge CB2 1EZ, UK; fax: +44(0)1223-336033.

Electronic supplementary information (ESI) available: Characterization, ^{1}H and ^{13}C NMR spectra, and crystallographic analysis report of DMPDI. FTIR spectrum of the prepared compounds. Comparison of DFT optimized geometrical parameters with X- ray crystal data structure, vibrational assignments of DMPDI and hyperpolarizability calculations. The online version of this article contains supplementary material, which is available to authorized users.

Disclosure statement

Conflict of interest: The authors declare that they have no conflict of interest associated with this article.
Ethical approval: All ethical guidelines have been adhered to.
Sample availability: Samples of the compounds are available from the author.

CRediT authorship contribution statement

Conceptualization: Kiran Pradhan, Mossaraf Hossain, Dhiraj Brahman, Anoop Kumar, Munna Mukhia; Methodology: Kiran Pradhan, Dhiraj Brahman, Anoop Kumar, Munna Mukhia, Sumiran Tamang, Sangita Dey; Validation: Kiran Pradhan, Mossaraf Hossain, Dhiraj Brahman, Anoop Kumar; Formal Analysis: Munna Mukhia, Sangita Dey, Sumiran Tamang, Koushik Chakraborty, Koustav Singha, Kiran Pradhan; Investigation: Kiran Pradhan, Mossaraf Hossain, Anoop Kumar, Sumiran Tamang, Munna Mukhia, Imran Habib; Resources: Kiran Pradhan, Mossaraf Hossain, Anoop Kumar, Dhiraj Brahman; Writing - Original Draft: Kiran Pradhan, Munna Mukhia, Dhiraj Brahman, Anoop Kumar; Writing - Review and Editing: Mossaraf Hossain, Kiran Pradhan, Dhiraj Brahman, Koustav Singha, Imran Habib, Koushik Chakraborty; Visualization: Kiran Pradhan, Mossaraf Hossain, Munna Mukhia.

ORCID and Email

Munna Mukhia
rs_munna@nbu.ac.in
https://orcid.org/0009-0002-3747-339X
Sumiran Tamang
sumirantamang12@gmail.com
https://orcid.org/0009-0006-5570-6264
Koushik Chakraborty
koushik.papai@gmail.com
https://orcid.org/0009-0008-8696-8077
Imran Habib
rs_imran@nbu.ac.in
https://orcid.org/0009-0003-9524-0292
Koustav Singha
rs_koustav@nbu.ac.in
https://orcid.org/0009-0008-8830-0687
Sangita Dey
rs_sangitad@nbu.ac.in
https://orcid.org/0009-0003-0076-6882
Anoop Kumar
anoop@nbu.ac.in
https://orcid.org/0000-0001-9061-9533
Dhiraj Brahman
dhirajslg@gmail.com
https://orcid.org/0000-0002-4613-0885
Mossaraf Hossain
mossarafchem@nbu.ac.in
https://orcid.org/0009-0004-5954-1562
Kiran Pradhan
kpradhan@nbu.ac.in
https://orcid.org/0000-0001-8484-0274

References

[1]. Lombardino, J. G.; Wiseman, E. H. Preparation and antiinflammatory activity of some nonacidic trisubstituted imidazoles. *J. Med. Chem.* **1974**, *17* (11), 1182–1188.

[2]. Alghamdi, S. S.; Suliman, R. S.; Almutairi, K.; Kahtani, K.; Aljatli, D. Imidazole as a Promising Medicinal Scaffold: Current Status and Future Direction. *Drug Des Devel Ther.* **2021**, *Volume 15*, 3289–3312.

[3]. Sharma, P.; LaRosa, C.; Antwi, J.; Govindarajan, R.; Werbovetz, K. A. Imidazoles as Potential Anticancer Agents: An Update on Recent Studies. *Molecules* **2021**, *26* (14), 4213.

[4]. Al-Badr, A. A.; Alodhaib, M. M. Dacarbazine. *Profiles Drug Subst. Excip. Relat. Methodol.* **2016**, *41*, 323–377.

[5]. Hume, A. L.; Kerkering, T. M. Ketoconazole (Nizoral, Janssen Pharmaceutica, Inc.). *Drug Intell. amp; Clin. Pharm.* **1983**, *17* (3), 169–174.

[6]. Goa, K. L.; Wagstaff, A. J. Losartan Potassium. *Drugs* **1996**, *51* (5), 820–845.

[7]. Finkelstein, W.; Isselbacher, K. J. Drug therapy: Cimetidine. N. *Engl. J. Med.* **1978**, *299*, 992–996.

[8]. Nakamura, S. Structure of Azomycin, a new antibiotic. *Pharm. Bull.* **1955**, *3*, 379–383.

[9]. Grimmett, M. R. Advances in Imidazole Chemistry. In Advances in Heterocyclic Chemistry; Elsevier, 1981; pp. 241–326.

[10]. Grimmett, M. R. Advances in Imidazole Chemistry. In Advances in Heterocyclic Chemistry Volume 12; Elsevier, 1970; pp. 103–183.

[11]. Dupont, J.; Suarez, P. A. Z. Physico-chemical processes in imidazolium ionic liquids. *Phys. Chem. Chem. Phys.* **2006**, *8*, 2441–2452.

[12]. Nikitina, P. A.; Perevalov, V. P. Methods of synthesis and physicochemical properties of 1-hydroxyimidazoles, imidazole 3-oxides, and their benzoannulated analogs. *Chem Heterocycl Comp* **2017**, *53* (2), 123–149.

[13]. Cerecetto, H.; Dias, E.; Di Maio, R.; González, M.; Pacce, S.; Saenz, P.; Seoane, G.; Suescun, L.; Mombrú, A.; Fernández, G.; Lema, M.; Villalba, J. Synthesis and Herbicidal Activity of *N*-Oxide Derivatives. *J. Agric. Food Chem.* **2000**, *48* (7), 2995–3002.

[14]. Witschel, M. Design, synthesis and herbicidal activity of new iron chelating motifs for HPPD-inhibitors. *Bioorg. amp; Med. Chem.* **2009**, *17* (12), 4221–4229.

[15]. Abuskhuna, S. M.; Zeglam, T. H.; Fhid, O. N.; Jebril, A. O. Antibacterial Activity of Hydroxyimidazole Derivatives. *Asian Jour. Pharm. and Technol.* **2020**, *10* (1), 7.

[16]. Allan, G. G.; Chopra, C. S.; Mattila, T. Imidazoles III. Pesticidal screening of some substituted 1-hydroxyimidazoles. *Pestic. Sci.* **1972**, *3* (2), 153–159.

[17]. Aguirre, G.; Boiani, M.; Cerecetto, H.; Gerpe, A.; González, M.; Sainz, Y. F.; Denicola, A.; de Ocáriz, C. O.; Nogal, J. J.; Montero, D.; Escario, J. A. Novel Antiprotozoal Products: Imidazole and Benzimidazole *N*-Oxide Derivatives and Related Compounds. *Arch. Pharm.* **2004**, *337* (5), 259–270.

[18]. Richardson, M. L.; Croughton, K. A.; Matthews, C. S.; Stevens, M. F. Structural Studies on Bioactive Compounds. 39. Biological Consequences of the Structural Modification of DHFR-Inhibitory 2,4-Diamino-6-(4-substituted benzylamino-3-nitrophenyl)-6-ethylpyrimidines ('benzoprims'). *J. Med. Chem.* **2004**, *47* (16), 4105–4108.

[19]. Alp, M.; Göker, H.; Ozkan, T.; Sunguroglu, A. Synthesis and cytotoxic evaluation of novel N-substituted amidino-1-hydroxybenzimidazole derivatives. *Arch. Pharm. Res.* **2013**, *37* (5), 580–587.

[20]. Bowser, T. E.; Bartlett, V. J.; Grier, M. C.; Verma, A. K.; Warchol, T.; Levy, S. B.; Alekshun, M. N. Novel anti-infection agents: Small-molecule inhibitors of bacterial transcription factors. *Bioorg. amp; Med. Chem. Lett.* **2007**, *17* (20), 5652–5655.

[21]. Dimova, D.; Iyer, P.; Vogt, M.; Totzke, F.; Kubbutat, M. H.; Schächtele, C.; Laufer, S.; Bajorath, J. Assessing the Target Differentiation Potential of Imidazole-Based Protein Kinase Inhibitors. *J. Med. Chem.* **2012**, *55* (24), 11067–11071.

[22]. Stensbøl, T. B.; Uhlmann, P.; Morel, S.; Eriksen, B. L.; Felding, J.; Kromann, H.; Hermit, M. B.; Greenwood, J. R.; Braüner-Osborne, H.; Madsen, U.; Junager, F.; Krogsgaard-Larsen, P.; Begtrup, M.; Vedsø, P. Novel 1-Hydroxyazole Bioisosteres of Glutamic Acid. Synthesis, Protolytic Properties, and Pharmacology. *J. Med. Chem.* **2001**, *45* (1), 19–31.

[23]. Wang, J. C. Cellular roles of DNA topoisomerases: a molecular perspective. *Nat Rev Mol Cell Biol* **2002**, *3* (6), 430–440.

[24]. Kadioglu, O.; Chan, A.; Cong Ling Qiu, A.; Wong, V. K.; Colligs, V.; Wecklein, S.; Freund-Henni Rached, H.; Efferth, T.; Hsiao, W. W. Artemisinin Derivatives Target Topoisomerase 1 and Cause DNA Damage in Silico and in Vitro. *Front. Pharmacol.* **2017**, *8*, 711 https://doi.org/10.3389/fphar.2017.00711.

[25]. Papadaki, C.; Karachaliou, N.; Lagoudaki, E.; Trypaki, M.; Sfakianaki, M.; Koutsopoulos, A.; Mavroudis, D.; Stathopoulos, E.; Georgoulias, V.; Souglakos, J. Predictive value of BRCA1, ERCC1, ATP7B, PKM2, TOPO-I, TOPO-iia, TOPO-iib, and c-MYC genes in patients with small cell lung cancer (SCLC) who received first-line therapy with cisplatin and etoposide. *J. Clinical Oncology* **2013**, *31* (15_suppl), 7594–7594.

[26]. Benzon, K.; Sheena, M. Y.; Panicker, C. Y.; Armaković, S.; Armaković, S. J.; Pradhan, K.; Nanda, A. K.; Van Alsenoy, C. Studies on the synthesis, spectroscopic analysis, molecular docking and DFT calculations on 1-hydroxy-2-(4-hydroxyphenyl)-4,5-dimethyl-imidazol 3-oxide. *J. Mol. Struct.* **2017**, *1130*, 644–658.

[27]. Sheldrick, G. M. A short history of*SHELX*. *Acta Crystallogr A. Found Crystallogr* **2007**, *64* (1), 112–122.

[28]. Sheldrick, G. M. [37] Patterson superposition and ab initio phasing. *Methods Enzymol.* **1997**, *276*, 628–641.

[29]. Farrugia, L. J. *ORTEP*-3 for Windows - a version of*ORTEP*-III with a Graphical User Interface (GUI). *J. Appl Crystallogr* **1997**, *30* (5), 565–565.

[30]. Spek, A. L. Structure validation in chemical crystallography. *Acta Crystallogr D. Biol Crystallogr* **2009**, *65* (2), 148–155.

[31]. Farrugia, L. J. *WinGX*suite for small-molecule single-crystal crystallography. *J. Appl Crystallogr* **1999**, *32* (4), 837–838.

[32]. Becke, A. D. Density-functional thermochemistry. III. The role of exact exchange. *J. Chem. Phys.* **1993**, *98* (7), 5648–5652.

[33]. Lee, C.; Yang, W.; Parr, R. G. Development of the Colle-Salvetti correlation-energy formula into a functional of the electron density. *Phys. Rev. B.* **1988**, *37* (2), 785–789.

[34]. Dennington, R.; Keith, T. A.; Millam, J. M. GaussView, Version 6, Semichem Inc.; Shawnee Mission, KS, 2016.

[35]. Mosmann, T. Rapid colorimetric assay for cellular growth and survival: Application to proliferation and cytotoxicity assays. *J. Immunol. Methods* **1983**, *65* (1-2), 55–63.

[36]. Eberhardt, J.; Santos-Martins, D.; Tillack, A. F.; Forli, S. AutoDock Vina 1.2.0: New Docking Methods, Expanded Force Field, and Python Bindings. *J. Chem. Inf. Model.* **2021**, *61* (8), 3891–3898.

[37]. Trott, O.; Olson, A. J. AutoDock Vina: Improving the speed and accuracy of docking with a new scoring function, efficient optimization, and multithreading. *J. Comput Chem* **2009**, *31* (2), 455–461.

[38]. Pettersen, E. F.; Goddard, T. D.; Huang, C. C.; Couch, G. S.; Greenblatt, D. M.; Meng, E. C.; Ferrin, T. E. UCSF Chimera—A visualization system for exploratory research and analysis. *J. Comput Chem* **2004**, *25* (13), 1605–1612.

[39]. Morris, G. M.; Huey, R.; Lindstrom, W.; Sanner, M. F.; Belew, R. K.; Goodsell, D. S.; Olson, A. J. AutoDock4 and AutoDockTools4: Automated docking with selective receptor flexibility. *J. Comput Chem* **2009**, *30* (16), 2785–2791.

[40]. BIOVIA Discovery Studio Visualizer, BIOVIA, Dassault Systèmes: San Diego, 2024.

[41]. Pradhan, S.; Gurung, P.; Chettri, A.; Singha, U. K.; Mishra, D. K.; Dutta, T.; Sinha, B. Investigation of DNA binding and antibacterial properties of a Zn(II) Complex with an N2OS Salophen-type Ligand. *J. Mol. Struct.* **2025**, *1339*, 142431.

[42]. Pradeep Kumar, M.; Tejaswi, S.; Rambabu, A.; Kalalbandi, V. K.; Shivaraj, Synthesis, crystal structure, DNA binding and cleavage studies of copper(II) complexes with isoxazole Schiff bases. *Polyhedron* **2015**, *102*, 111–120.

[43]. Gupta, R. K.; Sharma, G.; Pandey, R.; Kumar, A.; Koch, B.; Li, P.; Xu, Q.; Pandey, D. S. DNA/Protein Binding, Molecular Docking, and in Vitro Anticancer Activity of Some Thioether-Dipyrrinato Complexes. *Inorg. Chem.* **2013**, *52* (24), 13984–13996.

[44]. Spackman, M. A.; Jayatilaka, D. Hirshfeld surface analysis. *CrystEngComm* **2009**, *11* (1), 19–32.

[45]. DJ, G.; Sidden, C.; Paulraj, R.; Robert, H. M.; Ajitha, S. Structural, Hirshfeld surface analysis, third order non-linear optical and molecular modelling of imidazolium glutarate single crystals for optical applications. *J. Mol. Struct.* **2023**, *1276*, 134672.

[46]. Fucke, K.; Steed, J. W. X-ray and Neutron Diffraction in the Study of Organic Crystalline Hydrates. *Water* **2010**, *2* (3), 333–350.

[47]. Mary, Y. S.; Jojo, P.; Panicker, C. Y.; Van Alsenoy, C.; Ataei, S.; Yildiz, I. Theoretical investigations on the molecular structure, vibrational spectra, HOMO–LUMO and NBO analysis of 5-chloro-2-((4-chlorophenoxy)methyl)benzimidazole. *Spectrochim. Acta A: Mol. Biomol. Spectrosc.* **2014**, *122*, 499–511.

[48]. Belletête, M.; Morin, J.; Leclerc, M.; Durocher, G. A Theoretical, Spectroscopic, and Photophysical Study of 2,7-Carbazolenevinylene-Based Conjugated Derivatives. *J. Phys. Chem. A.* **2005**, *109* (31), 6953–6959.

[49]. Zhenming, D.; Heping, S.; Yufang, L.; Diansheng, L.; Bo, L. Experimental and theoretical study of 10-methoxy-2-phenylbenzo[h]quinoline. *Spectrochim. Acta A: Mol. Biomol. Spectrosc.* **2011**, *78* (3), 1143–1148.

[50]. Snehalatha, M.; Ravikumar, C.; Hubert Joe, I.; Sekar, N.; Jayakumar, V. Spectroscopic analysis and DFT calculations of a food additive

Carmoisine. *Spectrochim. Acta A: Mol. Biomol. Spectrosc.* **2009**, *72* (3), 654–662.
[51]. Chettri, S.; Tamang, S.; Rai, P.; Rai, Y.; Singha, U. K.; Pradhan, K.; Brahman, D.; Sinha, B. Synthesis, physico-chemical characterization and theoretical exploration of some 2,4,5-triaryl imidazole derivatives. *Journal of Heterocyclic Chem* **2023**, *60* (8), 1394–1415.
[52]. Koopmans, T. Über die Zuordnung von Wellenfunktionen und Eigenwerten zu den Einzelnen Elektronen Eines Atoms. *Physica* **1934**, *1* (1-6), 104–113.
[53]. Priya, M.; Zochedh, A.; Chandran, K.; Arumugam, K.; Banu, S.; Chakaravarthy, C.; Sultan, A. B. Computer-aided analysis of biochanin-A as a potential breast cancer drug based on DFT, molecular docking, and pharmacokinetic studies. *Letters in Applied NanoBioScience* **2023**, *12*, 165 https://nanobioletters.com/wp-content/uploads/2022/12/LIANBS124.165.pdf
[54]. Rani, V.; Pal Singh, B.; Kumar, A. Structural, NBO, HOMO-LUMO Analysis Using DFT and Molecular Docking Analysis of Bioactive 3,4-Difluoroacetophenone-Thiosemicarbazone as a Potential Anticancer Agent. *Nano LIFE* **2023**, *13* (03), 2350011 https://doi.org/10.1142/s1793984423500113.
[55]. Ayub, M. A.; Tyagi, A. R.; Srivastava, S. K.; Singh, P. Quantum DFT analysis and molecular docking investigation of various potential breast cancer drugs. *J. Mater. Chem. B.* **2025**, *13* (1), 218–238.
[56]. Parr, R. G.; Pearson, R. G. Absolute hardness: companion parameter to absolute electronegativity. *J. Am. Chem. Soc.* **1983**, *105* (26), 7512–7516.
[57]. Pearson, R. G. Chemical hardness and density functional theory. *J. Chem Sci* **2005**, *117* (5), 369–377.
[58]. Parr, R. G.; Szentpály, L. v.; Liu, S. Electrophilicity Index. *J. Am. Chem. Soc.* **1999**, *121* (9), 1922–1924.
[59]. Scrocco, E.; Tomasi, J. The electrostatic molecular potential as a tool for the interpretation of molecular properties. In Topics in Current Chemistry Fortschritte der Chemischen Forschung; Springer Berlin Heidelberg: Berlin, Heidelberg, 2007; pp. 95–170.
[60]. Jaramillo, P.; Pérez, P.; Contreras, R.; Tiznado, W.; Fuentealba, P. Definition of a Nucleophilicity Scale. *J. Phys. Chem. A.* **2006**, *110* (26), 8181–8187.
[61]. Roeges, N. P. G. A guide to the complete interpretation of infrared spectral of organic structures; John Wiley & Sons: Chichester, England, 1994.
[62]. Krishnakumar, V.; Muthunatesan, S. DFT studies of the structure and vibrational assignments of 4-hydroxy quinazoline and 2-hydroxy benzimidazole. *Spectrochim. Acta A: Mol. Biomol. Spectrosc.* **2007**, *66* (4-5), 1082–1090.
[63]. Raju, R.; Panicker, C. Y.; Nayak, P. S.; Narayana, B.; Sarojini, B.; Van Alsenoy, C.; Al-Saadi, A. A. FT-IR, molecular structure, first order hyperpolarizability, MEP, HOMO and LUMO analysis and NBO analysis of 4-[(3-acetylphenyl)amino]-2-methylidene-4-oxobutanoic acid. *Spectrochim. Acta A: Mol. Biomol. Spectrosc.* **2015**, *134*, 63–72.
[64]. Varghese, H. T.; Yohannan Panicker, C.; Philip, D.; Mannekutla, J. R.; Inamdar, S. IR, Raman and SERS studies of methyl salicylate. *Spectrochim. Acta A: Mol. Biomol. Spectrosc.* **2007**, *66* (4-5), 959–963.
[65]. Szabó, A.; Kovács, A. Structure and molecular vibrations of dimethylglyoxime. *J. Mol. Struct.* **2003**, *651-653*, 615–619.
[66]. Yadav, R. K.; Yadav, B.; Yadav, R. A.; Kostova, I. Experimental IR, Raman, and UV-Vis spectra DFT structural and conformational studies: Bioactivity and solvent effect on molecular properties of methyl-eugenol. *Molecules* **2023**, *28*, 5409.
[67]. Varasanyi, G. Assignments for Vibrational Spectra of Seven Hundred Benzene Derivatives, Vol. 2, Adam Hilger, John Wiley & Sons: Nashville, TN, 1974.
[68]. Silverstein, R. M.; Webster, F. X.; Kiemle, D. Spectrometric identification of organic compounds; 7th ed.; Wiley, 2014.
[69]. Nitrile oxides, nitrones & nitronates in organic synthesis: Novel strategies in synthesis; Feuer, H., Ed.; John Wiley & Sons, 2008.
[70]. Benzon, K.; Mary, Y. S.; Varghese, H. T.; Panicker, C. Y.; Armaković, S.; Armaković, S. J.; Pradhan, K.; Nanda, A. K.; Van Alsenoy, C. Spectroscopic, DFT, molecular dynamics and molecular docking study of 1-butyl-2-(4-hydroxyphenyl)-4,5-dimethyl-imidazole 3-oxide. *J. Mol. Struct.* **2017**, *1134*, 330–344.
[71]. Breuer, E.; etc. Nitrones, Nitronates and Nitroxides; Breuer, E.; Aurich, H. G.; Nielsen, A., Eds.; John Wiley & Sons: Chichester, England, 1989.
[72]. Forrester, A. R.; etc. Organic chemistry of stable free radicals; Academic Press: San Diego, CA, 1968.
[73]. Benzon, K.; Varghese, H. T.; Panicker, C. Y.; Pradhan, K.; Tiwary, B. K.; Nanda, A. K.; Alsenoy, C. V. Spectroscopic and theoretical characterization of 2-(4-methoxyphenyl)-4,5-dimethyl-1H-imidazole 3-oxide. *Spectrochim. Acta A: Mol. Biomol. Spectrosc.* **2015**, *151*, 965–979.
[74]. Lin-Vien, D.; Colthup, N. B.; Fateley, W. G.; Grasselli, J. G. The handbook of infrared and Raman characteristic frequencies of organic molecules; Academic Press: San Diego, CA, 1991.
[75]. Lambert, J. B.; Shurvell, H. F.; Verbit, L.; Cooks, R. G.; Stout, G. H. Organic Structural Analysis. Organic Structural Analysis 1976.
[76]. Hoffmann, A. K.; Henderson, A. T. A new stable free radical: di-t-butylnitroxide. *J. Am. Chem. Soc.* **1961**, *83* (22), 4671–4672.
[77]. Rintoul, L.; Micallef, A.; Reid, D.; Bottle, S. The vibrational spectrum of the stable free radical 1,1,3,3-tetramethylisoindolin-2-yloxyl. *Spectrochim. Acta A: Mol. Biomol. Spectrosc.* **2006**, *63* (2), 398–402.
[78]. Tanak, H.; Köysal, Y.; Ünver, Y.; Yavuz, M.; Işık, U.; Sancak, K. An experimental and DFT computational study on 4-(3-(1*H*-imidazol-1-yl)propyl)-5-methyl-2*H*-1,2,4-triazol-3(4*H*)-one monohydrate. *Mol. Phys.* **2010**, *108* (2), 127–139.
[79]. Genç, S.; Dege, N.; Çetin, A.; Cansız, A.; Şekerci, M.; Dinçer, M. 3-(2-Hydroxyphenyl)-4-phenyl-1*H*-1,2,4-triazole-5(4*H*)-thione. *Acta Crystallogr E. Struct Rep Online* **2004**, *60* (9), o1580–o1582.
[80]. Dani, A.; Groppo, E.; Barolo, C.; Vitillo, J. G.; Bordiga, S. Design of high surface area poly(ionic liquid)s to convert carbon dioxide into ethylene carbonate. *J. Mater. Chem. A.* **2015**, *3* (16), 8508–8518.
[81]. Hasegawa, K.; Ono, T.-A.; Noguchi, T. Vibrational spectra and ab initio DFT calculations of 4-methylimidazole and its different protonation forms: Infrared and Raman markers of the protonation state of a histidine side chain. *J. Phys. Chem. B* **2000**, *104*, 4253–4265.
[82]. Bhagyasree, J.; Varghese, H. T.; Panicker, C. Y.; Samuel, J.; Van Alsenoy, C.; Bolelli, K.; Yildiz, I.; Aki, E. Vibrational spectroscopic (FT-IR, FT-Raman, 1H NMR and UV) investigations and computational study of 5-nitro-2-(4-nitrobenzyl) benzoxazole. *Spectrochim. Acta A: Mol. Biomol. Spectrosc.* **2013**, *102*, 99–113.
[83]. Shakila, G.; Periandy, S.; Ramalingam, S. Vibrational spectroscopic investigation (FT-IR and FT-Raman) on 1,2-dibromobenzene by HF and hybrid (LSDA and B3LYP) calculations. *Spectrochim. Acta A: Mol. Biomol. Spectrosc.* **2011**, *86*, 449–455. https://doi.org/10.1016/j.saa.2011.10.066.
[84]. Socrates, G. Infrared and Raman Characteristics Group Frequency: Table and Charts. 3rd edition, John Wiley and Sons, 2006.
[85]. Felföldi, K.; Sutyinszky, M.; Nagy, N.; Pálinkó, I. Synthesis of *E*- and *Z*-*o*-Methoxy-Substituted 2,3-Diphenyl Propenoic Acids and Its Methyl Esters. *Synth. Commun.* **2000**, *30* (9), 1543–1553.
[86]. Ambujakshan, K.; Madhavan, V.; Varghese, H. T.; Panicker, C. Y.; Temiz-Arpaci, O.; Tekiner-Gulbas, B.; Yildiz, I. Vibrational spectroscopic studies and ab initio calculations of 5-methyl-2-(p-methylaminophenyl)benzoxazole. *Spectrochim. Acta A: Mol. Biomol. Spectrosc.* **2008**, *69* (3), 782–788.
[87]. Al-Wabli, R. I.; Al-Ghamdi, A. R.; Ghabbour, H. A.; Al-Agamy, M. H.; Monicka, J. C.; Joe, I. H.; Attia, M. I. Synthesis, X-ray single crystal structure, molecular docking and DFT computations on N-[(1E)-1-(2H-1,3-benzodioxol-5-yl)-3-(1H-imidazol-1-yl)propylidene]-hydroxylamine: A new potential antifungal agent precursor. *Molecules* **2017**, *22*, 373.
[88]. Wright, J. B. The Reaction between 2,3-Butanedione Monoxime and Aldehyde Oximes. The Preparation of 1-Hydroxyimidazoles 3-Oxides. *J. Org. Chem.* **1964**, *29* (6), 1620–1621.
[89]. Shen, Y. R. The principles of nonlinear optics; John Wiley & Sons: Nashville, TN, 2003.
[90]. Kolinsky, P. V. New materials and their characterization for photonic device applications. *Opt. Eng.* **1992**, *31* (8), 1676.
[91]. Eaton, D. F. Nonlinear Optical Materials. *Science* **1991**, *253* (5017), 281–287.
[92]. Krishnan, A.; Pal, S.; Nandakumar, P.; Samuelson, A.; Das, P. Ferrocenyl donor–organic acceptor complexes for second order nonlinear optics. *Chem. Phys.* **2001**, *265* (3), 313–322.
[93]. Kleinman, D. A. Nonlinear Dielectric Polarization in Optical Media. *Phys. Rev.* **1962**, *126* (6), 1977–1979.
[94]. Thanthiriwatte, K. S.; Nalin de Silva, K. Non-linear optical properties of novel fluorenyl derivatives—ab initio quantum chemical calculations. *J. Mol. Struct.: THEOCHEM* **2002**, *617* (1-3), 169–175.
[95]. Adant, C.; Dupuis, M.; Bredas, J. L. Ab initio study of the nonlinear optical properties of urea: Electron correlation and dispersion effects. *Int. J. Quantum Chem.* **1995**, *56* (S29), 497–507.
[96]. Laus, G.; Schwärzler, A.; Bentivoglio, G.; Hummel, M.; Kahlenberg, V.; Wurst, K.; Kristeva, E.; Schütz, J.; Kopacka, H.; Kreutz, C.; Bonn, G.; Andriyko, Y.; Nauer, G.; Schottenberger, H. Synthesis and Crystal Structures of 1-Alkoxy-3-alkylimidazolium Salts Including Ionic Liquids, 1-Alkylimidazole 3-oxides and 1-Alkylimidazole Perhydrates. *Z. fur Naturforsch. B* **2008**, *63* (4), 447–464.
[97]. Hengel, S. R.; Spies, M. A.; Spies, M. Small-Molecule Inhibitors Targeting DNA Repair and DNA Repair Deficiency in Research and Cancer Therapy. *Cell Chem. Biol.* **2017**, *24* (9), 1101–1119.
[98]. Pommier, Y.; Leo, E.; Zhang, H.; Marchand, C. DNA Topoisomerases and Their Poisoning by Anticancer and Antibacterial Drugs. *Chem. amp; Biol.* **2010**, *17* (5), 421–433.
[99]. Rahman, A.; O'Sullivan, P.; Rozas, I. Recent developments in compounds acting in the DNA minor groove. *Med. Chem. Commun.* **2019**, *10* (1), 26–40.
[100]. Singhal, S.; Khanna, P.; Khanna, L. Synthesis, DFT studies, molecular docking, antimicrobial screening and UV fluorescence studies on ct-

DNA for novel Schiff bases of 2-(1-aminobenzyl) benzimidazole. *Heliyon* **2019**, *5* (10), e02596.
[101]. Ahmad, I.; Ahmad, M. Dacarbazine as a minor groove binder of DNA: Spectroscopic, biophysical and molecular docking studies. *Int. J. Biol. Macromol.* **2015**, *79*, 193–200.
[102]. Mohamadi, M.; Yousef Ebrahimipour, S.; Torkzadeh-Mahani, M.; Foro, S.; Akbari, A. A mononuclear diketone-based oxido-vanadium(iv) complex: structure, DNA and BSA binding, molecular docking and anticancer activities against MCF-7, HPG-2, and HT-29 cell lines. *RSC. Adv.* **2015**, *5* (122), 101063–101075.
[103]. Jacob, J. M.; Mohan, N.; S. S. , S.; Sithambaresan, M.; Manoj, E.; Kurup, M. P. Multi-faceted investigation of copper(II) chelates based on ONS donor thiosemicarbazone: Crystal structures, spectral aspects, DNA binding, cytotoxicity and computational studies. *J. Mol. Struct.* **2025**, *1319*, 139463.
[104]. Saygıdeğer Demir, B.; İnce, S.; Yilmaz, M. K.; Sezan, A.; Derinöz, E.; Taskin-Tok, T.; Saygideger, Y. DNA Binding and Anticancer Properties of New Pd(II)-Phosphorus Schiff Base Metal Complexes. *Pharmaceutics* **2022**, *14* (11), 2409.
[105]. Ghosh, K.; Kumar, P.; Tyagi, N.; Singh, U. P.; Aggarwal, V.; Baratto, M. C. Synthesis and reactivity studies on new copper(II) complexes: DNA binding, generation of phenoxyl radical, SOD and nuclease activities. *Eur. J. Med. Chem.* **2010**, *45* (9), 3770–3779.
[106]. Long, E. C.; Barton, J. K. On demonstrating DNA intercalation. *Acc. Chem. Res.* **1990**, *23* (9), 271–273.
[107]. Liu, Z.; Wang, B.; Yang, Z.; Li, Y.; Qin, D.; Li, T. Synthesis, crystal structure, DNA interaction and antioxidant activities of two novel water-soluble Cu(2+) complexes derivated from 2-oxo-quinoline-3-carbaldehyde Schiff-bases. *Eur. J. Med. Chem.* **2009**, *44* (11), 4477–4484.
[108]. Meyer-Almes, F. J.; Porschke, D. Mechanism of intercalation into the DNA double helix by ethidium. *Biochemistry* **1993**, *32* (16), 4246–4253.
[109]. Heestand, G. M.; Schwaederle, M.; Gatalica, Z.; Arguello, D.; Kurzrock, R. Topoisomerase expression and amplification in solid tumours: Analysis of 24,262 patients. *Eur. J. Cancer* **2017**, *83*, 80–87.
[110]. Lee, Y.; Lee, C.; Tsai, H.; An, H.; Lee, C.; Wu, J.; Chen, C.; Huang, S.; Hwang, J.; Cheng, K.; Leiw, P.; Chen, C.; Lin, C. Targeting of Topoisomerase I for Prognoses and Therapeutics of Camptothecin-Resistant Ovarian Cancer. *PLoS ONE.* **2015**, *10* (7), e0132579.
[111]. Pommier, Y. DNA Topoisomerase I Inhibitors: Chemistry, Biology, and Interfacial Inhibition. *Chem. Rev.* **2009**, *109* (7), 2894–2902.
[112]. Nitiss, J. L. Targeting DNA topoisomerase II in cancer chemotherapy. *Nat Rev Cancer* **2009**, *9* (5), 338–350.
[113]. Pommier, Y.; Sun, Y.; Huang, S. N.; Nitiss, J. L. Roles of eukaryotic topoisomerases in transcription, replication and genomic stability. *Nat Rev Mol Cell Biol* **2016**, *17* (11), 703–721.
[114]. Daina, A.; Michielin, O.; Zoete, V. SwissADME: a free web tool to evaluate pharmacokinetics, drug-likeness and medicinal chemistry friendliness of small molecules. *Sci Rep* **2017**, *7* (1), 42717 https://doi.org/10.1038/srep42717.
[115]. Labby, K. J.; Xue, F.; Kraus, J. M.; Ji, H.; Mataka, J.; Li, H.; Martásek, P.; Roman, L. J.; Poulos, T. L.; Silverman, R. B. Intramolecular hydrogen bonding: A potential strategy for more bioavailable inhibitors of neuronal nitric oxide synthase. *Bioorg. Med. Chem.* **2012**, *20* (7), 2435–2443.
[116]. Wang, S.; König, G.; Roth, H.; Fouché, M.; Rodde, S.; Riniker, S. Effect of Flexibility, Lipophilicity, and the Location of Polar Residues on the Passive Membrane Permeability of a Series of Cyclic Decapeptides. *J. Med. Chem.* **2021**, *64* (17), 12761–12773.
[117]. Ritchie, T. J.; Ertl, P.; Lewis, R. The graphical representation of ADME-related molecule properties for medicinal chemists. *Drug Discov. Today* **2011**, *16* (1-2), 65–72.
[118]. Lucas, A. J.; Sproston, J. L.; Barton, P.; Riley, R. J. Estimating human ADME properties, pharmacokinetic parameters and likely clinical dose in drug discovery. *Expert Opin. Drug Discov.* **2019**, *14* (12), 1313–1327.